Intrinsic Contact Sensing and Object Perception of an Adaptive Fin-Ray Gripper Integrating Compact Deflection Sensors

Genliang Chen, *Member, IEEE*, Shujie Tang, Shaoqiu Xu, Tong Guan, Yuanhao Xun, Zhuang Zhang, *Member, IEEE*, Hao Wang, and Zhongqin Lin

***Abstract*—Owing to their tremendous adaptability to free-form objects, soft grippers with fin-ray structure have a wide range of applications. However, kinetostatics analysis and contact sensing for such soft grippers are quite a challenge due to large structural deformations. In this article, a model-based method for intrinsic contact sensing, object perception, and interactive manipulation, is proposed for this kind of adaptive grippers. The contributions arise from the integration of compact strain-gauge sensors, that are particularly fabricated for slender flexible beams undergoing large deformations. Using a discretization-based approach, the contact condition can be identified efficiently in light of the local deformations gathered via the deflection sensors. Prototypes are developed using simple materials and manufacturing methods, on which various validation experiments are conducted. Owing to the contact sensing capability, the developed adaptive fin-ray gripper is able to perceive the boundary geometry and structural compliance of unstructured objects. Moreover, sensor-based feed-back control can be accomplished to perform interactive manipulation, in which the contact force between the finger and object can be regulated precisely (around 5 % RMS error) in real-time.**

***Index Terms*—Adaptive fin-ray gripper, deflection sensors, intrinsic contact sensing, kinetostatics analysis, object perception.**

I. Introduction

STRUCTURAL compliance is of vital importance for robot grippers to perform robust and stable grasping, especially for fragile and deformable objects [1], [2], [3], [4], [5]. Soft grippers with the so-called fin-ray structure [6] exhibit a simple yet reliable way to permit compliant interaction with the grasping objects. As illustrated in Fig. 1, the tremendous adaptability of such a fin-ray gripper arises from the passive structural deformations of its flexible components to conform to the touching surface. Owing to this merit, pioneered by Festo [7], various adaptive grippers composing of fin-ray fingers have been developed to handle a wide range of objects with free-form shapes [8], [9], [10]. Although such a fin-ray gripper is simple in structure, easy to fabricate and of high passive compliance, it is quite a challenge to develop an accurate and efficient model to characterize its kinetostatics behavior in contact with objects.

As exhibited in Fig. 1, the flexible components of the fin-ray fingers undergo large-scale deformations when in contact with an object. Moreover, these slender flexible beams are mutually supported by several rigid ribs via passive joints, which results in a complex multiloop mechanism composing of flexible and rigid links. As a consequence, the conventional approaches for compliant/flexible mechanisms, including the classical elliptic integrals approach [11], [12], [13], the pseudorigid-body technique [14], [15], [16], and the Cosserat rod method [17], [18], [19], [20], cannot be directly applied to the kinetostatics modeling and analysis of these fin-ray fingers. Therefore, in the literature, there is a lack of comprehensive study on the kinetostatics analysis of these fin-ray grippers. As a generic approach, finite element method (FEM) is adopted to simulate the structural deformations of the fin-ray fingers under different loading conditions [21], [22]. However, subject to the computational burden, FEM is usually employed for the structural optimization, rather than real-time kinetostatics analysis of those adaptive grippers, in spite of its high-precision accuracy. To this issue, Shan and Birglen [23] provided an analytical formulation to the kinetostatics using the pseudorigid-body method. In their model, a fin-ray finger is roughly approximated by a multibody system (MBS), and the kinetostatics analysis can be implemented via MBS simulation. Recently, Armanini et al. [24] introduced the discrete Cosserat rod approach to the kinetostatics modeling of fin-ray effect fingers and applied it to both the deformation analysis and parametric optimization of such adaptive fingers.

Apart from accurate kinetostatics models, the ability of force sensing is also of vital importance to such fin-ray grippers for real-time control [2], [25], which can significantly improve the

Manuscript received 30 March 2023; revised 1 July 2023; accepted 25 August 2023. Date of publication 19 September 2023; date of current version 6 December 2023. This paper was recommended for publication by Associate Editor V. Ho and Editor E. Yoshida upon evaluation of the reviewers' comments. This work was supported in part by the National Key R&D Program of China under Grant 2019YFA0709000, in part by the Natural Science Foundation of China (NSFC) under Grant 52022056, Grant 52205031, and in part by Zhejiang Lab Open Research Project under Grant K2022NB0AB03. *(Corresponding author: Genliang Chen.)*

Genliang Chen and Shujie Tang are with the Meta Robotics Institute, State Key Laboratory of Mechanical System and Vibration, Shanghai Jiao Tong University, Shanghai 200240, China (e-mail: leungchen@gmail.com; sjtang@sjtu.edu.cn).

Shaoqiu Xu, Tong Guan, Yuanhao Xun, Hao Wang, and Zhongqin Lin are with the State Key Laboratory of Mechanical System and Vibration, Shanghai Key Laboratory of Digital Manufacturing for Thin-Walled Structures, Shanghai Jiao Tong University, Shanghai 200240, China (e-mail: shaoqiuxu@sjtu.edu.cn; tongguan@sjtu.edu.cn; 1056411499@qq.com; wanghao@sjtu.edu.cn; zqlin@sjtu.edu.cn).

Zhuang Zhang is with the Westlake University, Hangzhou, Zhejiang 310024, China (e-mail: z.zhang@sjtu.edu.cn).

This article has supplementary material provided by the authors and color versions of one or more figures available at https://doi.org/10.1109/TRO.2023.3311610.

Digital Object Identifier 10.1109/TRO.2023.3311610

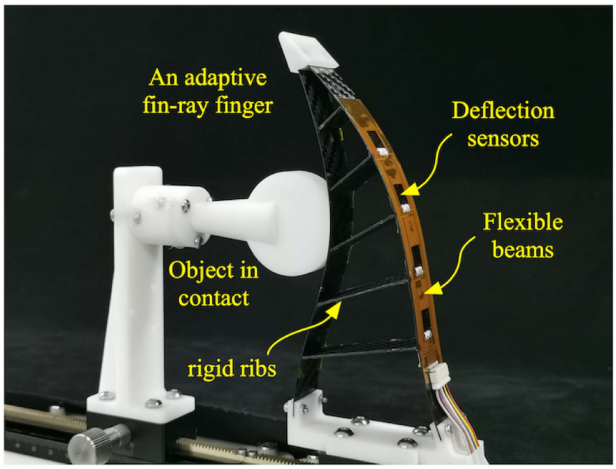

Fig. 1. Adaptive fin-ray finger integrating compact deflection sensors.

performance of interactive grasping with the objects. However, due to large structural deformations, traditional proprioceptive sensors (such as encoders, force/torque gauges) are difficult to be embedded into the flexible components. To this end, many alternative techniques of force sensing for the fin-ray grippers have been reported in the literature.

Abdeetedal and Kermani [26] presented a sensorized adaptive gripper with the capability of obtaining the contact force and location via a compact load cell embedded in the finger phalanxes. To conform the large deformations, Basson and Bright [27] attached flexible force-sensitive film resistors to the soft fin-ray gripper to directly detect the grasping density for active haptic control. Aiming at physical human-robot interaction, Mahsereci et al. [28] integrated high-resolution flexible tactile sensors to the adaptive grippers to enhance perception of object recognition. An ultra-thin CMOS stress sensor is particularly developed by Mahsereci et al. [29] for the fin-ray grippers to enable the extraction of object shapes and manipulation status. Recently, vision-based approaches, usually in conjunction with deep learning techniques, are emerging for the force sensing of adaptive grippers. By embedding interior cameras into soft fingers, She et al. [30] developed the vision-based sensor, GelFlex, to simultaneously obtain the proprioceptive and tactile data undergoing large deformations. Similarly, using neural network method, Xu et al. [31] also introduced a vision-based force sensing approach for the traditional fin-ray grippers by inserting rigid rods as reference nodes. Relying on the recent progress of image-based deep learning techniques, De Barrie et al. [32] established a learning-based framework for predicting the contact force and stress distribution of the fin-ray grippers. Although the vision-based methods are robust for force sensing, extra cameras were required to capture the images. This significantly increases the complexity of gripper system, especially in space limited scenarios, even difficult to implement in those soft fin-ray fingers. Moreover, the training of the neural network, usually relying on FEM simulation, also imposes additional computational burden.

In this article, a model-based sensing method is proposed for predicting the contact condition of the adaptive fin-ray gripper [7], in the light of local deformations gathered at a number of discrete positions. To this end, a special type of strain gauge sensors is particularly designed and fabricated for the flexible beams in the soft gripper that undergoing large deformation. A systematic kinetostatics model of the studied fin-ray structure is established in the discretization-based modeling framework, developed in our prior work [33], for large deflection problems of slender flexible links. The benefit of this modeling strategy results from the approximation of flexible beams to articulated mechanisms with a large number of rigid bodies and passive elastic joints. Conventional methods for robot kinematics and statics can be adopted to complete the kinetostatics modeling and analysis, as well as contact sensing of the studied fin-ray structure. Using the proposed model, the contact condition of the adaptive gripper can be predicted precisely and efficiently, such that object perception can be realized.

To verify the feasibility of the proposed model-based contact sensing and object perception, a prototype of the adaptive fin-ray gripper is developed utilizing easy-to-access materials and simple fabrication approaches. And a variety of experiments are conducted on the developed fin-ray gripper to validate the effectiveness of the established modeling, analysis, and sensing methods. The results show that, according to the deformation data collected by the locally-deployed deflection sensors, the developed adaptive gripper can predict the touch condition and contact force in comparatively high precision and efficiency. In addition, the gripper's capabilities of geometry reconstruction and compliance perception of unstructured object are exhibited in an intuitive way. Furthermore, demonstrations on interactive manipulation of the developed adaptive fin-ray gripper are also given to verify the capability of sensor-based feedback control of contact force.

The rest of this article is organized as follows. Section II presents the mechanical design and prototyping of the studied adaptive fin-ray gripper. A general approach for the elastostatics of large-deformation flexible beams is also introduced in this section, as the modeling framework. Then, the kinetostatics modeling for the fin-ray fingers is conducted in Section III, where contact-enforced deformation analysis is also completed. In Section IV, a model-based sensing method is established for identifying the equilibrium configurations in contact with objects. Section V conducts a variety of experiments to verify the correctness and effectiveness of the proposed modeling, analysis, and contact sensing methods. In this section, the capabilities of geometry reconstruction and compliance perception of the unstructured objects are validated for the developed adaptive fin-ray gripper. Thereafter, interactive manipulation in contact with both fixed and moving objects are provide in Section VI, to demonstrate the efficiency and applicability of the established contact sensing method. Finally, Section VII concludes the article.

II. Prototyping and Modeling Framework

This section presents the mechanical design and fabrication of the studied adaptive soft gripper. Easy-to-access materials and simple fabrication approaches are used to make the flexible and rigid components, as well as the passive connecting joints.

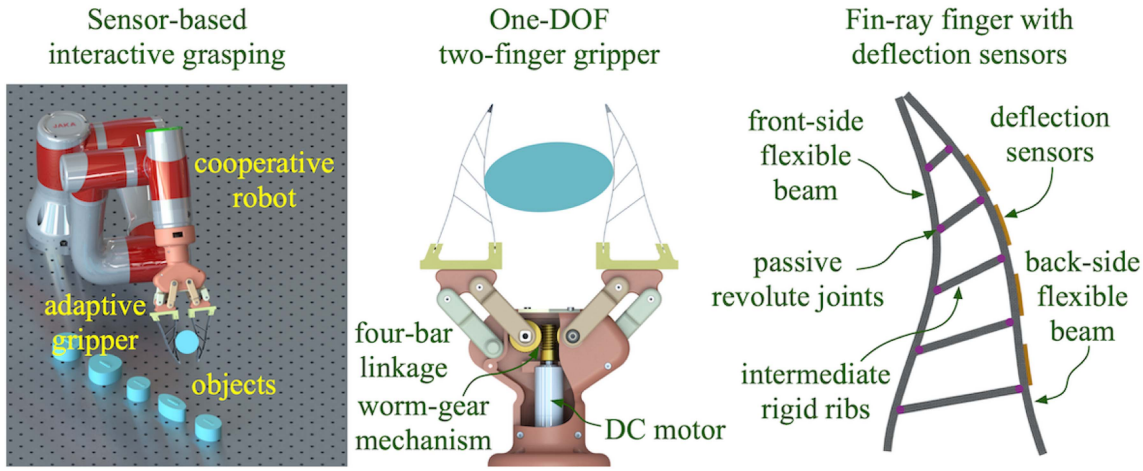

Fig. 2. Architecture of the studied adaptive fin-ray gripper integrating deflection sensors.

A modeling framework for the elastostatics of slender flexible beams that undergoing large-scale deformations is introduced in this section for the kinetostatics modeling and analysis of the soft fingers with the fin-ray structure.

A. Architecture Characterization and Fabrication Method

As shown in Fig. 2, the studied adaptive gripper composes of two identical soft fingers with fin-ray structure. These two fingers are actuated by two planar four-bar linkages that driven via a common worm-gear mechanism. The developed adaptive gripper is mounted on the end-effector of a cooperative robotic arm, JAKA-Zu3, to perform grasping tasks. Compared to the existing fin-ray grippers, the main contribution of the proposed one is the integration of the compact deflection sensors locally deployed on the back-side flexible beam. As a consequence, model-based prediction for contact conditions with the grasped objects can be realized in a precise and efficient way.

As same as the widely-used fin-ray grippers [7], the studied soft finger consists of two slender flexible beams, denoted by the "front-side" and "back-side" beams, respectively, as shown in Fig. 2. These two flexible beams are mutually supported by a number of intermediate rigid ribs via passive revolute joints. Owing to this special fin-ray structure, such a soft finger can deform passively to accommodate the shape of the objects in contact, which would result in a simple and reliable grasping. Comprehensive study on the analysis and optimization of these fin-ray grippers have been conducted in the literature [7], [11]. In this article, we focus on kinetostatic modeling and analysis, and contact sensing of these soft fin-ray fingers. Therefore, the kinematic parameters of the developed soft fin-ray fingers are determined according to the criterion proposed in [21].

As shown in Fig. 3, an asymmetric structure is adopted in this article. The length l_0 and angle φ_0 specify the finger's size and shape. The compliance characteristics mainly depends on the number of rigid supporting ribs, namely r, and their positions and orientations, namely l_i and φ_i, for $i = 1, \ldots, r$. In addition, the capability of contact sensing for the developed finger relies on the number of the deployed deflection sensors,

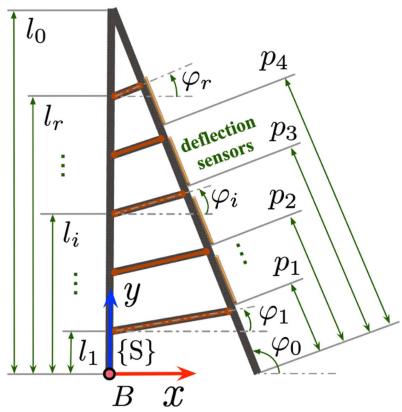

Fig. 3. Kinematic parameters of the studied fin-ray fingers.

TABLE I
KINEMATIC PARAMETERS OF THE DEVELOPED FIN-RAY FINGER

Symb.	value (mm)	Symb.	value (°)	Symb.	value (mm)
l_0	140	φ_0	112	p_0	/
l_1	17	φ_1	10	p_1	30
l_2	39	φ_2	13	p_2	53
l_3	61	φ_3	16	p_3	76
l_4	83	φ_4	19	p_4	98
l_5	105	φ_5	22	/	/

termed m, and their positions on the back-side beam, namely p_j $(j = 1, \ldots, m)$. The values of these kinematic parameters of the developed fin-ray fingers are listed in Table I.

The existing methods for manufacturing the adaptive fin-ray grippers can be categorized into two types. On one hand, the soft fingers can be fully 3-D printed as a whole structure using multiple materials [23], [32]. Although 3-D printing is a very convenient way to fabricate the fin-ray fingers, the printed materials suffer from plastic deformation after repeated usage. Moreover, it is also difficult to derive an accurate elastostatics

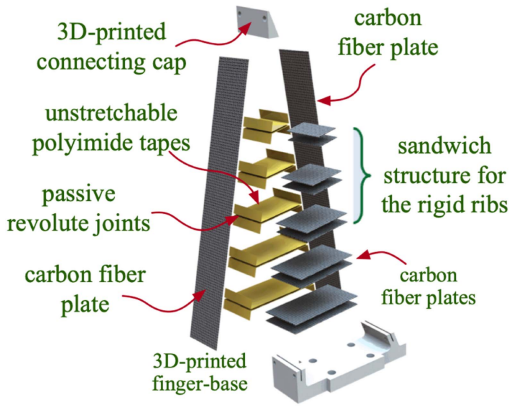

Fig. 4. Fabrication of the adaptive fin-ray fingers.

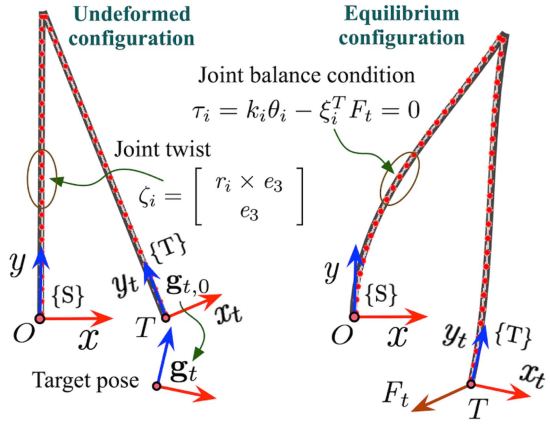

Fig. 5. Elastostatics modeling of the finger's flexible component.

model for the printed plastic structure. On the other hand, the flexible beams and rigid ribs can also be fabricated separately and assemble together to construct the finger [7], [24]. In such a case, passive hinges are required to connect the supporting ribs to the flexible beams. Then, assembling positions on both the rigid ribs and the flexible beams should be reserved, which results in an incompact structure and noncontinuous flexible characteristics. And this will also increase the difficulty to the elastostatics modeling of the soft fingers.

To this end, easy-to-access materials and simple fabrication techniques are used to manufacture the adaptive fin-ray fingers developed in this article. As shown in Fig. 4, both the flexible beams and the rigid ribs of the developed fingers are made of ordinary carbon-fiber plates. Meanwhile, soft yet unstretchable polyimide tapes are employed to fabricate flexure hinge joints [34], [35] with compact format. In addition, a sandwich structure is introduced to enhance the rigidness of the intermediate supporting ribs. Besides, both the finger base and the distal cap connecting the front-side and the back-side flexible beams are using 3-D printed plastic components.

As exhibited in Fig. 4, it is quite convenient to assembly all the above components together. The intermediate rigid ribs are acquired by clipping two face-to-face layers of polyimide tape with two identical carbon-fiber plates. In this step, regular glue for carbon-fiber materials are strong enough to bond the sandwich structure. Next, the fin-ray skeleton of the soft finger can be realized by means of adhering the polyimide tape to the flexible beams directly. In the end, the entire fin-ray finger can be achieved by attaching the flexible beams to each other, via the connecting cap at the distal ends, and mounting them to the finger base at the proximal ends. To ease the assembling procedures, simple customized 3-D printed molds are made to assist the manufacture of the soft fin-ray fingers.

The advantages of the developed fabrication method reflect in the following aspects. First, all the above components, e.g., the carbon-fiber plates, the polyimide tape, and the 3-D printed parts, can be acquired readily. Second, the relative rotation between the rigid ribs and the flexible beams are realized by the deflection of the unstretchable tap. Thus, the flexure hinges are more aligned with passive revolute joints. In addition, the adopted fabrication approaches lead to a compact structure, so that these adaptive fin-ray fingers can be easily miniaturized. Lastly, the flexible components are made of carbon-fiber plates in regular shapes (with a rectangular cross-section), which can be modeled more accurately using the established mechanism approximation approach.

B. *Framework for Elastostatics Modeling of Flexible Beams*

As addressed in Section II-A, the front and the back sides of the studied soft finger are made of slender carbon-fiber plates that can undergo large deformations. Thus, the prediction accuracy of the gripper's grasping behavior is significantly affected by the elastostatics models established for slender flexible beams. In this article, a discretization-based method for large deflection problems of flexible links, developed in our prior work [33], is introduced as the modeling framework for the characterization of elastostatics behavior of the slender flexible beams.

Using the proposed modeling method, a flexible beam will be discretized into a number of small elastic segments, whose structural compliances are approximated by articulated rigid-body linkages with passive elastic joints. Hence, the flexible beams can be characterized by hyperredundant multibody systems (MBS) composing of rigid bodies and elastic joints. The main advantage of the proposed modeling strategy comes from the approximation to the structural continuum mechanics with the kinetostatics of a rigid MBS. Therefore, conventional methods for robot kinematics and statics can be employed to accomplish the kinetostatics analysis concisely and efficiently. Refer to [36] for details of this method.

Since the distal end of the approximation mechanism is cut from the fixed base, geometric constraints should be imposed to the linkage's tip frame. As well, the balance condition in the joint space should be satisfied as the approximation joints are elastic. In the proposed method, the product-of-exponential formula is adopted for the kinematics and statics modeling of this hyperredundant rigid MBS, which results in a concise and straightforward representation [37].

As illustrated in Fig. 5, let $\{\mathrm{S}\}$ be the spatial frame as the system reference, and $\{\mathrm{T}\}$ the body-fixed tip frame attached to

the distal end. Then, the geometric constraint to the tip end of the approximation mechanism can be represented as follows:

$$\mathbf{g}_{st}(\boldsymbol{\theta}) = \exp(\hat{\boldsymbol{\zeta}}_1\theta_1)\cdots\exp(\hat{\boldsymbol{\zeta}}_n\theta_n)\,\mathbf{g}_{st,0} = \mathbf{g}_t \tag{1}$$

where $\mathbf{g}_{st} \in SE(3)$ denotes the relative pose of $\{\mathrm{T}\}$ with respect to $\{\mathrm{S}\}$, with $\mathbf{g}_{st,0} = \mathbf{g}_{st}(\mathbf{0})$ and $\mathbf{g}_t$ being the initial and the target ones, respectively. $\hat{\boldsymbol{\zeta}}_i \in se(3)$, $i = 1, \ldots, n$ are the joint twists, in 4×4 standard representation. $\boldsymbol{\theta} = [\theta_1, \ldots, \theta_n] \in \mathbb{R}^{n\times 1}$ is the vector of joint variables, whose components θ_i correspond to the displacements of the elastic joints.

Meanwhile, the equilibrium condition in the joint space can be stated as that, the restoring torques in those passive elastic joints must be balanced by the external load-induced reactions transmitted from the tip frame. Based on the reciprocal relation between motion and force transmission, the balance condition can be expressed in a concise form as follows:

$$\boldsymbol{\tau} = \mathbf{K}_{\boldsymbol{\theta}}\,\boldsymbol{\theta} - \mathbf{J}_t^T\,\boldsymbol{F}_t = \mathbf{0} \tag{2}$$

where $\mathbf{K}_{\boldsymbol{\theta}} = \mathrm{diag}(k_1, \ldots, k_n) \in \mathbb{R}^{n\times n}$ is the diagonal stiffness matrix of the elastic joints. $\boldsymbol{F}_t \in \mathbb{R}^{6\times 1}$ relates to the interaction force, in 6×1 wrench form, reacted between the mechanism and the fixed base at $\{\mathrm{T}\}$. $\mathbf{J}_t \in \mathbb{R}^{6\times n}$ is the Jacobian matrix relating the joint space to the tip frame.

By differentiating the POE Formula (1), the Jacobian matrix in (2) can be derived directly in a compact form as follows:

$$(\dot{\mathbf{g}}_{st}\mathbf{g}_{st}^{-1})^{\vee} = \mathbf{J}_t\,\dot{\boldsymbol{\theta}} \;\Rightarrow\; \mathbf{J}_t = [\boldsymbol{\xi}_1,\ \boldsymbol{\xi}_2,\ \cdots,\ \boldsymbol{\xi}_n] \tag{3}$$

where $(\,\cdot\,)^{\vee}$ is the "vee" operator mapping elements of $se(3)$ from the standard representation to vector form. And $\boldsymbol{\xi}_i \in \mathbb{R}^{6\times 1}$ simply relates to the corresponding joint twist, in the current configuration at $\boldsymbol{\theta}$, which can be obtained directly as follows:

$$\boldsymbol{\xi}_i = \mathrm{Ad}\left(\exp(\hat{\boldsymbol{\zeta}}_1\theta_1)\cdots\exp(\hat{\boldsymbol{\zeta}}_{i-1}\theta_{i-1})\right)\boldsymbol{\zeta}_i,\quad i = 1, \ldots, n$$

where $\mathrm{Ad}(\,\cdot\,)$ is the adjoint operator for $SE(3)$ [38].

Combining the geometric constraint to $\{\mathrm{T}\}$ and the equilibrium condition in the joint space, the kinetostatics model of the approximation mechanism can be written in the form of a set of nonlinear algebraic equations as follows:

$$\boldsymbol{C}(\boldsymbol{\theta},\,\boldsymbol{F}_t) = \begin{bmatrix}\boldsymbol{y}\\ \boldsymbol{\tau}\end{bmatrix} = \begin{bmatrix}\left(\ln(\mathbf{g}_{st}\,\mathbf{g}_t^{-1})\right)^{\vee}\\ \mathbf{K}_{\boldsymbol{\theta}}\,\boldsymbol{\theta} - \mathbf{J}_t^T\,\boldsymbol{F}_t\end{bmatrix} = \mathbf{0} \tag{4}$$

where $\boldsymbol{y} = (\ln(\mathbf{g}_{st}\,\mathbf{g}_t^{-1}))^{\vee} \in \mathbb{R}^{6\times 1}$ represents the pose deviation of the tip frame from its target one. While $\boldsymbol{\tau} \in \mathbb{R}^{n\times 1}$ relates to the deviation of torques that are restored in the elastic joints to balance the external load.

The kinetostatics model (4) relates to a set of $6+n$ nonlinear algebraic equations in terms of $n+6$ unknowns. It should be noted that, the planar pose $\mathbf{g}_{st}$ degenerates to elements belonging to the 3-D subgroup. Analogously, the reaction force $\boldsymbol{F}_t$ also degenerates a 3-D planar wrench. Hence, both the numbers of the valid equations and the independent variables are $n+3$, which implies that the kinetostatics model is deterministic. In the proposed model, the classical Newton-Raphson method is adopted to solve the obtained nonlinear algebraic equations in an efficient way, by making full use of system Jacobian matrix in analytical form.

Differentiating (4) with respect to all unknowns, the system Jacobian matrix of the kinetostatics model can be derived in a concise form as follows:

$$\boldsymbol{\nabla}_{\boldsymbol{C}} = \begin{bmatrix}\frac{\partial \boldsymbol{y}}{\partial \boldsymbol{\theta}} & \frac{\partial \boldsymbol{y}}{\partial \boldsymbol{F}_t}\\ \frac{\partial \boldsymbol{\tau}}{\partial \boldsymbol{\theta}} & \frac{\partial \boldsymbol{\tau}}{\partial \boldsymbol{F}_t}\end{bmatrix} = \begin{bmatrix}\mathbf{J}_t & \mathbf{0}\\ \mathbf{K}_{\boldsymbol{\theta}} - \mathbf{K}_{\mathbf{J}_t} & -\mathbf{J}_t^T\end{bmatrix} \tag{5}$$

where all the block elements are determined analytically in a straightforward way. Please refer to [36] for details.

On the basis of the analytical system Jacobian matrix (5), the equilibrium configuration (4) can then be determined in an iterative way by following the update theme as follows:

$$\begin{bmatrix}\boldsymbol{\theta}\\ \boldsymbol{F}_t\end{bmatrix}_{k+1} = \begin{bmatrix}\boldsymbol{\theta}\\ \boldsymbol{F}_t\end{bmatrix}_{k} + (\boldsymbol{\nabla}_{\boldsymbol{C}})_k^{-1}\,\boldsymbol{C}_k \tag{6}$$

where the subscript "k" denotes the k th iterative step.

According to (6), both the joint displacements $\boldsymbol{\theta}$ and the reaction force $\boldsymbol{F}_t$ will be repeatedly updated until they converge to stable values and the kinetostatics condition $\boldsymbol{C}$ approaches to zero. And the resultant configuration simply corresponds to the solution of the kinetostatics model of the approximation mechanism. The effectiveness and efficiency of the presented discretization-based approach has been validated in [36], [39], [40], [41], [42]. And it also works well for the "∧"-shape flexible beams in the studied adaptive fin-ray finger, as exhibited in Fig. 5, under the geometric constraint to the tip frame.

III. Kinetostatics Modeling and Analysis

On the basis of the modeling framework for the elastostatics of slender flexible beams, addressed in Section II-B, this section presents the kinetostatics modeling and analysis of the studied adaptive soft finger, with multiple intermediate supporting ribs. Further, the equilibrium condition of the soft finger in contact with a specified object is also established using the proposed method. The advantage of the presented modeling framework reflects that the kinetostatics model for single flexible beams can be extended to the whole finger naturally, even in the case of contact with objects.

As addressed in Section II-A, the flexible beams of the studied fin-ray finger are supported via multiple rigid intermediate ribs. Let L_k and R_k ($k = 1, \ldots, r$) be the connecting points on the front and the back beams that associated with the same rib, as shown in Fig. 6. Here, r is the number of ribs. Then, except for $\boldsymbol{y}$ and $\boldsymbol{\tau}$ in (4), extra constraints should be introduced to the approximation mechanism as follows:

$$d_k = \|\boldsymbol{r}_{L_k} - \boldsymbol{r}_{R_k}\| = d_{k,0},\quad k = 1, \ldots, r \tag{7}$$

where $d_{k,0}$ is the length of the rib. $\boldsymbol{r}_{L_k} \in \mathbb{R}^{3\times 1}$ and $\boldsymbol{r}_{R_k} \in \mathbb{R}^{3\times 1}$ are position vectors of L_k and R_k, respectively, in $\{\mathrm{S}\}$.

According to the reciprocal relationship between motion and force transmission, an internal reaction force will be generated in each of these supporting ribs. As addressed in Section II-A, these rigid ribs are connected to the flexible beams through unstretchable tapes, which can be regarded as compact passive revolute joints. Then, these fin-ray ribs can be considered as rigid two-force members, in which only a pure reaction force along the direction will be generated in each rib.

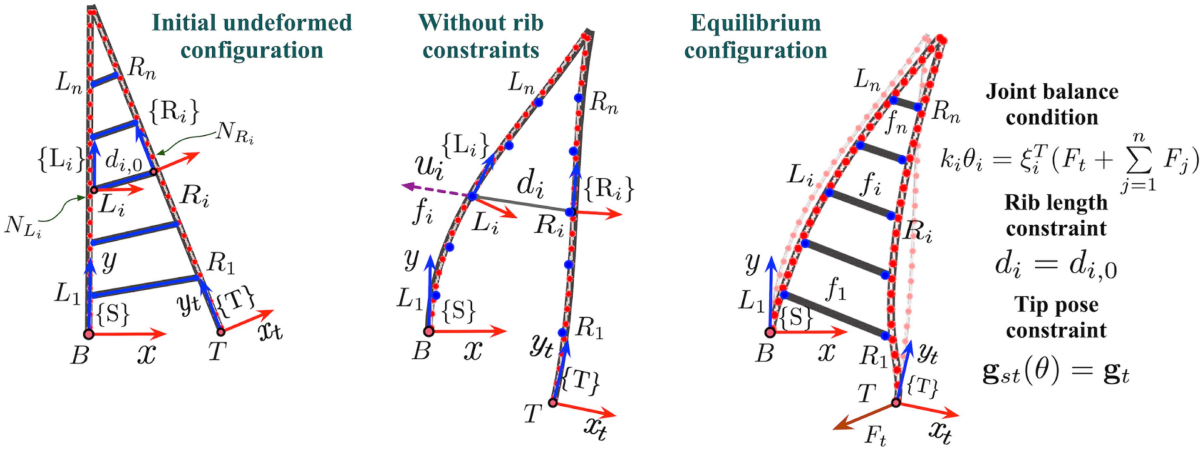

Fig. 6. Kinetostatics model of the whole fin-ray finger with the multiloop topology.

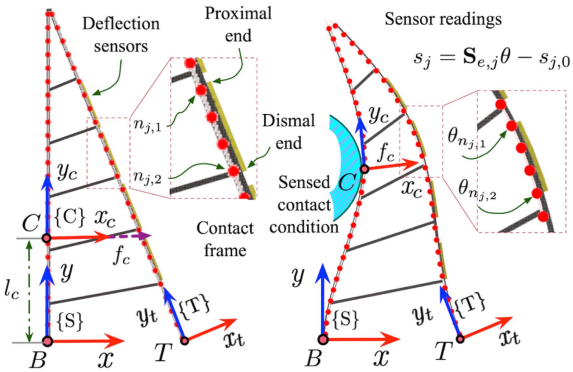

Fig. 7. Sensing model of contact condition.

As a result, these internal reaction forces can be expressed in the general form of 6×1 wrench as follows:

$$\boldsymbol{F}_k = f_k \begin{bmatrix} \boldsymbol{r}_{L_k} \times \boldsymbol{u}_k \\ \boldsymbol{u}_k \end{bmatrix} = f_k \boldsymbol{W}_k, \quad k = 1, \ldots, r \tag{8}$$

where $\boldsymbol{u}_k = (\boldsymbol{r}_{L_k} - \boldsymbol{r}_{R_k})/d_k$ corresponds to the unit vector from L_k to R_k. While $f_k \in \mathbb{R}$ is the magnitude of the reaction force and $\boldsymbol{W}_k$ is the corresponding unit wrench.

In such a scenario, the approximation mechanism of the soft finger is not only exerted by the reaction force at the tip frame, but also the internal ones reacted in the supporting ribs. Then, the balance condition in the joint space of the approximation mechanism, namely (2), should be updated by means of adding these additional ones as follows:

$$\boldsymbol{\tau} = \mathbf{K}_{\boldsymbol{\theta}}\boldsymbol{\theta} - \mathbf{J}_t^T \boldsymbol{F}_t - \sum_{k=1}^{r} \left(\mathbf{J}_{L_k}^T - \mathbf{J}_{R_k}^T\right) \boldsymbol{F}_k = \mathbf{0} \tag{9}$$

where $\mathbf{J}_{L_k} \in \mathbb{R}^{6\times n}$ and $\mathbf{J}_{R_k} \in \mathbb{R}^{6\times n}$ denote the Jacobian matrices of $\{\mathrm{L_k}\}$ and $\{\mathrm{R_k}\}$ with respect to $\{\mathrm{S}\}$, respectively.

It is worth noting that, for ease of representation, r pairs of local reference frames are constructed. As shown in Fig. 6, these local frames, denoted by $\{\mathrm{L_k}\}$ and $\{\mathrm{R_k}\}$, respectively, are attached to the back- and front-side flexible beams at L_k and R_k. Using the POE formula, these local Jacobian matrices in (9) can be obtained directly by picking up the corresponding columns from $\mathbf{J}_t$ as follows:

$$\begin{cases} \mathbf{J}_{L_k} = \left[\boldsymbol{\xi}_1, \ldots, \boldsymbol{\xi}_{n_{L_k}}, \mathbf{0}, \ldots, \mathbf{0}\right] \\ \mathbf{J}_{R_k} = \left[\boldsymbol{\xi}_1, \ldots, \boldsymbol{\xi}_{n_{R_k}}, \mathbf{0}, \ldots, \mathbf{0}\right] \end{cases}, \quad k = 1, \ldots, r \tag{10}$$

where n_{L_k} and n_{R_k} relate to the numbers of joints in front of $\{\mathrm{L_k}\}$ and $\{\mathrm{R_k}\}$, respectively. They can be determined directly according to the positions of the ribs.

For the sake of simplifying the representation, 4×1 homogeneous coordinates are utilized to depict the position vectors of the connecting points. Then, we have

$$\begin{cases} \overline{\boldsymbol{r}}_{L_k} = \mathbf{g}_{L_k}\, \overline{\boldsymbol{e}}_0 \\ \overline{\boldsymbol{r}}_{R_k} = \mathbf{g}_{R_k}\, \overline{\boldsymbol{e}}_0 \end{cases} \Rightarrow \begin{cases} \mathbf{g}_{L_k}(\boldsymbol{\theta}) = \prod_{k=1}^{n_{L_k}} \exp(\hat{\boldsymbol{\zeta}}_k \theta_k)\, \mathbf{g}_{L_k,0} \\ \mathbf{g}_{R_k}(\boldsymbol{\theta}) = \prod_{k=1}^{n_{R_k}} \exp(\hat{\boldsymbol{\zeta}}_k \theta_k)\, \mathbf{g}_{R_k,0} \end{cases} \tag{11}$$

where $\overline{\boldsymbol{r}}_{L_k} \in \mathbb{R}^{4\times 1}$ and $\overline{\boldsymbol{r}}_{R_k} \in \mathbb{R}^{4\times 1}$ represent the homogeneous coordinates of the point L_i and R_i, respectively, with respect to $\{\mathrm{S}\}$. $\mathbf{g}_{L_k} \in SE(3)$ and $\mathbf{g}_{R_k} \in SE(3)$ are the relative poses of $\{\mathrm{L_k}\}$ and $\{\mathrm{R_k}\}$ with respect to $\{\mathrm{S}\}$, having $\mathbf{g}_{R_k,0}$ and $\mathbf{g}_{L_k,0}$ as their initial poses. And $\overline{\boldsymbol{e}}_0 = [0, 0, 0, 1]^T$ corresponds to the homogeneous coordinates of the local origin.

Integrating the constraints of the rigid ribs (7) and updating the balance condition of the passive elastic joints with (9), the kinetostatics model of the whole fin-ray finger with rigid ribs can be represented in the form of implicit nonlinear algebraic equations as follows:

$$\boldsymbol{C}(\boldsymbol{\theta}, \boldsymbol{F}_t, \boldsymbol{f}) = \begin{bmatrix} \boldsymbol{y} \\ \boldsymbol{\tau} \\ \boldsymbol{d} \end{bmatrix} = \mathbf{0} \tag{12}$$

where $\boldsymbol{f} = [f_1, \ldots, f_r]^T \in \mathbb{R}^{r\times 1}$ is the vector of magnitudes of the internal forces. $\boldsymbol{d} = [d_1 - d_{1,0}, \ldots, d_r - d_{r,0}]^T \in \mathbb{R}^{r\times 1}$ is the deviation vector of the connecting distances from the lengths of the corresponding ribs.

The updated kinetostatic model (12) can be thought of as an extension of the original one (4), by introducing r additional

constraint functions $\boldsymbol{d}$ and an extra n-dimension unknown $\boldsymbol{f}$. Obviously, the number of equations still equals to the number of unknown variables. Thus, the Newton-Raphson method can be adopted again to solve the nonlinear algebraic equations in an iterative way. Analogously, the system Jacobian matrix of the updated nonlinear algebraic (12) can be derived in an analytical form. Moreover, all the block elements in (5) can be directly reused in the updated one.

The system Jacobian matrix of the implicit nonlinear algebraic (12) can be represented as follows:

$$\boldsymbol{\nabla}_{\boldsymbol{C}} = \begin{bmatrix} \frac{\partial \boldsymbol{y}}{\partial \boldsymbol{\theta}} & \frac{\partial \boldsymbol{y}}{\partial \boldsymbol{F}_t} & \frac{\partial \boldsymbol{y}}{\partial \boldsymbol{f}} \\ \frac{\partial \boldsymbol{\tau}}{\partial \boldsymbol{\theta}} & \frac{\partial \boldsymbol{\tau}}{\partial \boldsymbol{F}_t} & \frac{\partial \boldsymbol{\tau}}{\partial \boldsymbol{f}} \\ \frac{\partial \boldsymbol{d}}{\partial \boldsymbol{\theta}} & \frac{\partial \boldsymbol{d}}{\partial \boldsymbol{F}_t} & \frac{\partial \boldsymbol{d}}{\partial \boldsymbol{f}} \end{bmatrix} = \begin{bmatrix} \mathbf{J}_t & \mathbf{0} & \mathbf{0} \\ \mathbf{K}_{\boldsymbol{\theta}} - \mathbf{K}_{\mathbf{J}} & -\mathbf{J}_t^T & \frac{\partial \boldsymbol{\tau}}{\partial \boldsymbol{f}} \\ \frac{\partial \boldsymbol{d}}{\partial \boldsymbol{\theta}} & \mathbf{0} & \mathbf{0} \end{bmatrix} \tag{13}$$

where all the block elements can be derived analytically in the proposed modeling framework.

First, the item $\partial \boldsymbol{\tau}/\partial \boldsymbol{f}$ can be obtained by means of partially differentiating (9) with respect to $\boldsymbol{f}$ as

$$\begin{aligned} \frac{\partial \boldsymbol{\tau}}{\partial \boldsymbol{f}} &= -\frac{\partial}{\partial \boldsymbol{f}} \left(\sum_{k=1}^{r} (\mathbf{J}_{L_k} - \mathbf{J}_{R_k})^T \boldsymbol{W}_k \, f_k \right) \\ &= \left[\mathbf{J}_{W_1}^T \boldsymbol{W}_1, \, \ldots, \, \mathbf{J}_{W_r}^T \boldsymbol{W}_r \right] \end{aligned}$$

where $\mathbf{J}_{W_k} = \mathbf{J}_{R_k} - \mathbf{J}_{L_k} = [\ldots, \mathbf{0}, \boldsymbol{\xi}_{n_{L_k}}, \ldots, \boldsymbol{\xi}_{n_{R_k}}, \mathbf{0}, \cdots] \in \mathbb{R}^{6 \times n}$, which can be obtained directly by picking up the n_{L_k} to n_{R_k} columns from $\mathbf{J}_t$.

Besides, the newly-introduced item $\partial \boldsymbol{d}/\partial \boldsymbol{\theta}$ and the updated configuration-dependent one of the overall joint stiffness $\mathbf{K}_{\mathbf{J}}$ can also be derived analytically in a straightforward manner. The details of deduction for these partial derivative items can be found in Appendix A.

Taking advantage of the closed-form system Jacobian (13), the equilibrium configuration of the soft finger considering the multiple supports by the rigid fin-ray ribs can be determined iteratively using the Newton-Raphson method. Here, the same example of slender flexible beams given in Section II-B is adopted again to show the effectiveness of the proposed approach. As exhibited in Fig. 6, the static equilibrium configuration of the whole finger can be determined, once the constraint (12) are satisfied. From the figure, it can be seen that, under the geometric constraints of the intermediate supporting ribs, the equilibrium configuration of the fin-ray finger is different from the single flexible beam.

IV. Model-Based Sensing of Contact Condition

In Section III, the kinetostatics modeling and analysis of the studied adaptive finger with the fin-ray structure is conducted. Although the prediction of the contact-enforced deformation of the finger can be accomplished, it relies on the information on the object's shape and position. However, in many cases, the objects cannot be specified in advance and the kinetostatics analysis cannot be performed directly. To this end, strain-gauge sensors are particularly developed to measure the bending of the finger at multiple locations on its back-side beam. With this extra information, additional constraints can be imposed to the kinetostatics model, such that the information of the object can be released as unknown variables. Then, the contact condition can be sensed indirectly by means of the kinetostatics analysis in light of the sensor readings.

A. Deformation Reconstruction and Force Sensing

As shown in Fig. 7, m deflection sensors are deployed on the finger's back-side beam. As indicated in Section II-A, these deflection sensors are a special kind of strain gauges that are suitable for large-scale deformations. And their resistances are approximately proportional to their bending angles. Owing to this property, a sensing model of the contact condition can be established readily on the basis of its kinetostatics ones.

In this case, the flexible beams are enforced to deform due to the contact force reacted between the object and the finger. Accordingly, the balance condition (9) in the joint space of the approximation mechanism should be updated as follows:

$$\boldsymbol{\tau} = \mathbf{K}_{\boldsymbol{\theta}} \boldsymbol{\theta} - \mathbf{J}_t^T \boldsymbol{F}_t - \sum_{k=1}^{r} \left(\mathbf{J}_{L_k}^T - \mathbf{J}_{R_k}^T \right) \boldsymbol{F}_k - \mathbf{J}_c^T \boldsymbol{F}_c = \mathbf{0} \tag{14}$$

where $\mathbf{J}_c = [\boldsymbol{\xi}_1, \ldots, \boldsymbol{\xi}_{n_c}, \mathbf{0}, \ldots, \mathbf{0}] \in \mathbb{R}^{6 \times n}$ is the Jacobian matrix associated with the contact frame $\{\mathrm{C}\}$. Here, $n_c \in \mathbb{N}$ denotes the number of joints before $\{\mathrm{C}\}$, which is a function of contact position. And the contact force $\boldsymbol{F}_c \in \mathbb{R}^{6 \times 1}$ can be given as follows:

$$\boldsymbol{F}_c = f_c \begin{bmatrix} \boldsymbol{r}_C \times \boldsymbol{x}_c \\ \boldsymbol{x}_c \end{bmatrix} = f_c \boldsymbol{W}_c \tag{15}$$

where f_c denotes the magnitude of the contact force and $\boldsymbol{W}_c$ is the corresponding unit wrench. Here, $\boldsymbol{r}_C \in \mathbb{R}^{3 \times 1}$ and $\boldsymbol{x}_c \in \mathbb{R}^{3 \times 1}$ simply relate to the position of contact point C and $\boldsymbol{x}$-axis of $\{\mathrm{C}\}$, respectively. It is worth noting that the friction along the $\boldsymbol{y}_c$-axis is not taken into account.

In the proposed method, the bending angle of a deflection sensor simply corresponds to the sum of joint displacements it covers. Then, the bending information collected by the sensors can be added as an extra constraint as follows:

$$\boldsymbol{s} = \mathbf{S}_e \boldsymbol{\theta} - \boldsymbol{s}_0 = \mathbf{0} \tag{16}$$

where $\boldsymbol{s}_0 = [s_{1,0}, \ldots, s_{m,0}]^T \in \mathbb{R}^{m \times 1}$ corresponds to the readings of the deflection sensors. $\mathbf{S}_e \in \mathbb{R}^{m \times n}$ is a constant relating to the position of the sensors, whose rows are given by

$$\mathbf{S}_{e,j} = [0, \ldots, 0, 1, \ldots, 1, 0, \ldots, 0], \, j = 1, \ldots, m$$

whose $n_{j,1} \sim n_{j,2}$ elements are ones and the others are zeros. Here, $n_{j,1}$ and $n_{j,2}$ are the numbers of joints in front of the sensor's proximal and distal ends, respectively.

Substituting the balance condition in (12) with the updated one (14), the kinetostatic model of contact sensing can then be obtained by combining the sensor constraint (16), as follows:

$$\boldsymbol{C}(\boldsymbol{\theta}, \, \boldsymbol{F}_t, \, \boldsymbol{f}, \, l_c, \, f_c) = \begin{bmatrix} \boldsymbol{y} \\ \boldsymbol{\tau} \\ \boldsymbol{d} \\ \boldsymbol{s} \end{bmatrix} = \mathbf{0} \tag{17}$$

wherre l_c relates to the location of $\{\mathrm{C}\}$, as shown in Fig. 7.

In the sensing model (17), the contact conditions, including the location l_c and the magnitude f_c, are additional variables that need to be identified. On the other hand, the sensor information (16) induces additional constraints to the kinetostatic model. To make it solvable, at least two deflection sensors are required to be deployed on the back-side beam. As for the developed gripper, four sensors are deployed to increase the robustness of the proposed contact sensing method. Then, the number of equations is slightly greater than that of unknowns, such that the contact sensing model corresponds to an overdetermined problem. In such cases, the Newton-like algorithm will result in a least-square solution, which can reduce the influence of the measurement noise on the sensing accuracy.

Moreover, the system Jacobian matrix corresponding to (17) can be derived conveniently. The first and third rows just keep the same as the corresponding ones in (13). As for the last row, all block elements but the first one, including the partial derivatives of $\boldsymbol{s}$ with respect to $\boldsymbol{F}_t$, $\boldsymbol{f}$, l_c, and f_c yield to zeros, since the sensing reading is independent of them. Moreover, the partial derivative $\partial \boldsymbol{s}/\partial \boldsymbol{\theta}$ is simply the constant matrix $\mathbf{S}_e$. The remaining elements can be derived straightforwardly in a similar way, which are given in Appendix B.

Then, the Newton-like method can be used to determine the equilibrium configuration of the adaptive finger, as well as the contact condition, following the update theme:

$$\begin{bmatrix} \boldsymbol{\theta} \\ \boldsymbol{F}_t \\ \boldsymbol{f} \\ l_c \\ f_c \end{bmatrix}_{k+1} = \begin{bmatrix} \boldsymbol{\theta} \\ \boldsymbol{F}_t \\ \boldsymbol{f} \\ l_c \\ f_c \end{bmatrix}_{k} + (\boldsymbol{\nabla_C})_k^+ \boldsymbol{C}_k \tag{18}$$

where $(\boldsymbol{\nabla_C})_k^+$ is the pseudoinverse of Jacobian $\boldsymbol{\nabla_C}$ to (17).

Since the corresponding system Jacobian matrix is obtained analytically, the update theme (18) converges efficiently within several iterative steps. Then, the equilibrium configuration of the deformed soft finger can be reconstructed in terms of the identified joint variables. Similarly, the contact frame can also be determined according to its initial position on the front-side beam of the adaptive fin-ray finger. It should be noted that, in the proposed sensing model, the identified result only provides local information of the object geometry at the contact point. More precisely, the origin of the contact frame $\{\mathrm{C}\}$ locates on the boundary of the unknown object, while the corresponding tangent direction is simply coincident with $\boldsymbol{y}_c$-axis. Moreover, the contact force $\boldsymbol{F}_c$ is assumed in the normal direction, viz. $\boldsymbol{x}_c$-axis, and passing through the contact point. In other words, the shearing friction is not taken into account in the sensing model. An instance is provided in Fig. 7 to exhibit the reconstruction of the equilibrium configuration of the soft finger in contact with an unknown object.

B. Geometry Construction of Unknown Objects

As shown in Section IV-A, using the proposed sensing model, the deformed configuration of the finger's front-side beam, as well as the contact position, can be reconstructed. Then, the local information of object shape, which is locally consistent to the finger deformation around the contact location, can be determined. More precisely, for each contact configuration, a small curve that is internally tangent to the object surface, can be extracted for the contact position. As a result, the geometry of the entire object can be completely reconstructed through multiple touches from different orientations.

As illustrated in Fig. 8, by rotating the object to a number of discrete orientations, a bunch of common tangent curves can be locally collected from the deformed front-side beam around the contact position. Then, the interior envelope of these short curves can be extracted to depict the entire shape of the target object. In this article, image processing techniques are adopted to obtain the contour of the blank area enclosed by the tangent curves. As shown in the figure, the obtained contour fits the interior envelope of the tangent curves press well, such that it is extracted as the sensed shape of the unknown object. It should be noted that, in the proposed model, only those objects with smooth edges are taken into consideration.

For ease of description, the concept of Fourier descriptors for plane closed curves [43] is employed to depict the shape of the constructed object. Then, the contour of the object can be represented in the discrete Fourier expansion as follows:

$$\boldsymbol{f}(t) = \sum_{k=-K}^{K} c_k \, e^{i \cdot 2\pi k t}, \quad t = [0,\ 1] \tag{19}$$

where $c_k \in \mathbb{C}$ are the discrete Fourier coefficients, which can be obtained as $c_k = \sum_{n=0}^{N-1} e^{-i \cdot 2\pi k t} \boldsymbol{r}(n) \Delta t$. Here, N is the number of discrete points on the extracted envelope, then $\Delta t = 1/N$. $\boldsymbol{r}(n) \in \mathbb{C}$ relates to the coordinates of the n th point.

In the following section, a variety of objects with different shapes are tested using the proposed contact sensing method. The capability of the developed adaptive fin-ray fingers to reconstruct the geometry of unknown objects has been verified via these validation experiments.

C. Compliance Perception of Unstructured Objects

As indicated in the above, using the contact sensing model, the interaction force between the object and the finger can also be determined simultaneously with the contact position. Then, a compliance prediction model for objects with elasticity can be established by means of pushing the soft finger towards the object in different trials.

As shown in Fig. 9, a linear slider springily-connected to the ground is introduced to simulate the unstructured objects having structural compliance. In order to reduce the influence of friction, a pulley bearing is mounted on the slider to contact with the finger. Using the sensing model, the displacement of the slider and the corresponding contact force can be identified by pushing the finger with different strokes. Then, the stiffness of the elastic object can be represented in a general form as follows:

$$k_{o,\,x} = \frac{\Delta f_x}{\Delta x} \tag{20}$$

where $k_{o,\,x}$ represents the contact stiffness of the object at x. And $f_x = f_c \, \boldsymbol{x}^T \boldsymbol{x}_c$ corresponds to the linear component of the contact force along the slider direction.

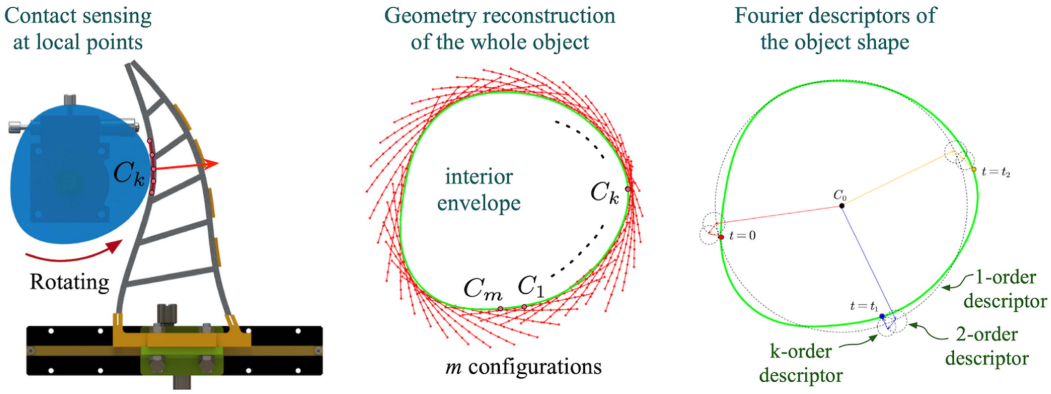

Fig. 8. Sensor-based construction of the object geometry.

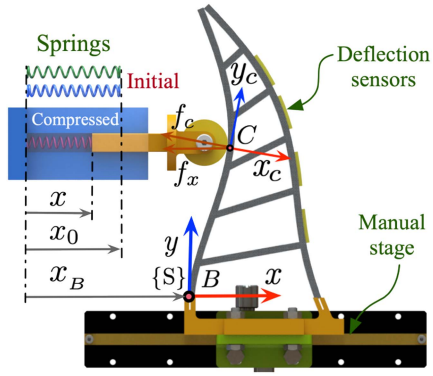

Fig. 9. Sensor-based perception of object compliance.

According to (20), the directional compliance of the elastic object can be predicted. Then, interactive control of the adaptive soft gripper can be performed to manipulate unstructured objects with structural compliance. Although the compliance prediction model developed in this section is particularly built for objects constrained to a linear slider, it can be extended to cases of free objects grasped via a two-finger gripper.

In Section V, corresponding experiments will be conducted on single fingers to validate the effectiveness of the obtained compliance prediction model for springy objects. As well, further demonstrations on compliance perception of unstructured compliant objects are provided on a two-finger gripper to exhibit the advantages of the established intrinsic contact sensing methodology.

D. Discussion

The capability of contact sensing is established based on the exact kinetostatic model of the adaptive fin-ray gripper. As it is known, the kinetostatic model of such a flexible robotic system is determined under the condition of prescribed contact state. Owing to the information gathered by the deflection sensors, extra equations can be obtained to release the contact condition as unknown variables. This gives the adaptive gripper the capability of intrinsic contact sensing and object perception. In the proposed method, each sensor measures the corresponding local deformation of the flexible beam as a whole. Therefore, it requires at least two deflection sensors to identify the contact condition (location plus force) for each point. In the developed grippers, four strain gauges are integrated in the large fingers for validation experiments, and three are used in the smaller ones for interactive grasping. Consequently, in this paper, only the single-point model is developed and implemented. This is the main limitation of the proposed contact sensing method for the adaptive fin-ray gripper.

To overcome this limitation, two methods can be potentially adopted to realize contact sensing of multiple points. On one hand, more strain gauges can be used on the back-side beam, as well the front-side one, to gather more abundant information of local deformations. Thus, more equations can be derived to achieve multipoint contact sensing. On the other hand, data-driven methods can be introduced to establish the input/output relation between the sensor readings and the contact condition of multiple points. Hence, the contact information of multiple points can also be estimated, even with less deflection sensors, using the proposed sensing method integrated in the adaptive fin-ray gripper. The aforementioned two ways will be further studied in our future work, to enhance the sensing capability of the developed adaptive gripper.

V. Experimental Validation

In the section, different types of experiments are conducted to verify the effectiveness of the proposed modeling, analysis, and sensing methods for the studied adaptive fin-ray structure. As exhibited in Section II-A, using easy-to-access materials and simple fabrication approaches, a prototype of the soft adaptive gripper is developed for the validation experiments. From the results, it can be seen that, owing to the local deformation data collected by the deflection sensors, the proposed discretization-based method works well for the kinetostatics analysis of the adaptive soft fingers in contact with objects.

A. Experimental Setup

To accomplish the validation experiments for the proposed modeling, analysis, and contact sensing methods, an apparatus

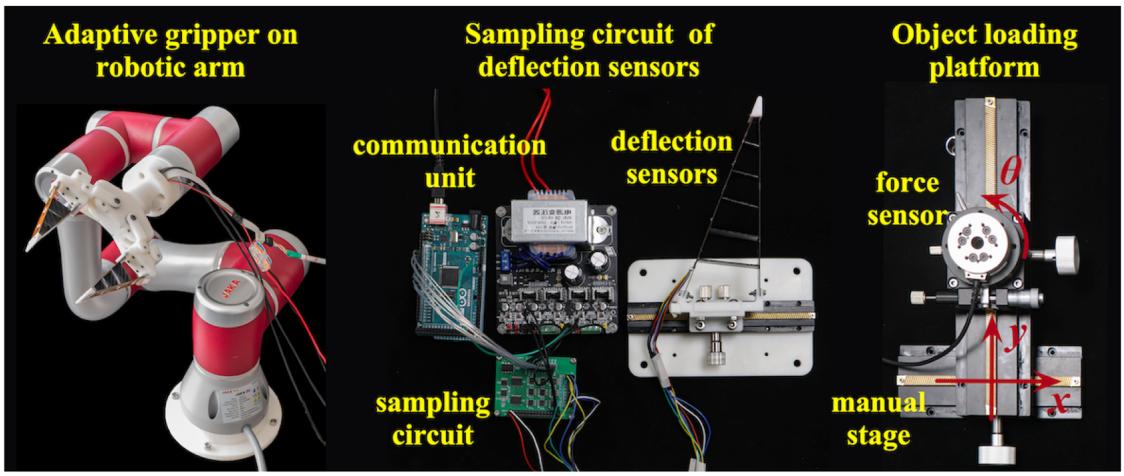

Fig. 10. Experimental setup for the validation of the proposed contact sensing methodology.

is particularly designed and built up, composing of the soft fin-ray fingers, a two-finger gripper, the deflection-sensing device, and a manual object-loading platform. As shown in Fig. 10, the whole experimental setup can be divided into the following four subsystems.

a) The adaptive gripper with fin-ray fingers: As addressed in Section II-A, fiber-carbon plates and unstretchable polyimide tapes are adopted to construct the slender flexible beams, the intermediate rigid ribs, and the passive revolute joints. Besides, a one-DOF fully actuated gripper composing of two fin-ray fingers is fabricated mainly using 3-D printed plastic components and a worm-gear mechanism actuated by a high-quality Maxon dc motor.

b) The sensing subsystem for local deflections: Full-bridge strain gauges for large-scale bending are deployed on the back-side flexible beams of the soft fingers. And a sampling circuit integrating multiple transmission channels is designed to collect the information of local deformations, in real-time, from the gauge sensors.

c) The implementation subsystem for kinetostatics analysis: The calculation algorithm for contact sensing model of the soft fin-ray gripper is implemented using C++ language. Hence, the solution procedures for kinetostatics analysis and contact sensing can run efficiently at about 30 Hz. An interface is developed to communicate with the deflection sensing module and the servo controller of the gripper.

d) The object loading platform: A planar 3-DOF platform is constructed using commercial three high-precision manual stages, as shown in Fig. 10. Then, the object can be loaded from different positions and orientations to contact with the soft finger. Besides, an ATI force/torque sensor is deployed on the loading platform as an external sensor to measure the interaction force between the target object and the soft finger.

In the developed experimental setup, the SoftBUS technique is employed to integrate all the above subsystems, including the kinetostatics analysis module, the dc motor controller, the deflection sensing circuit, and the ATI F/T sensor. Therefore, all those datum in the validation experiments can be collected and transferred in an automatic way. This provides the reliable hardware/software support for the developed adaptive gripper to perform object perception in real-time.

B. Validation of Kinetostatics Analysis and Contact Sensing

In this section, based on the developed experimental setup, various experiments are carried out to validate the proposed kinetostatics modeling and analysis. As shown in Fig. 10, a sliding platform is used to load a circular object to contact with the finger at a series of specific positions. In these validation experiments, a 4×6 grid of workspace is prescribed for the target object. For each position, the deformed configuration of the flexible beams and the corresponding resistance reading of the deflection sensors are recorded simultaneously. Meanwhile, the theoretical results of these contact condition are calculated using the developed kinetostatics model. Then, comparisons of the contact locations and reaction forces between the predicted ones and those measured in the experiments are made for the validation of the model-based contact sensing method.

Fig. 11 shows the pose deviations of the predicted contact frames from the measured ones. In this experiment, the exact configurations of these frames measured between the object and the finger are captured via an image processing method. From the results, it can be seen that the proposed kinetostatics model is able to characterize the contact-deformation behavior of the studied fin-ray finger. The mean position and orientation errors of the calculated contact frames are 0.70 mm and 1.21°, respectively, at the 24 tested locations. Analogously, the poses of the contact frames obtained using the model-based sensing method are also illustrated in the figure. Correspondingly, the mean position and orientation errors of the predicted contact frames are 0.58 mm and 1.24°, respectively, from the measured ones. The results verify the feasibility and effectiveness of the proposed model-based prediction method for contact sensing of the developed adaptive fin-ray gripper.

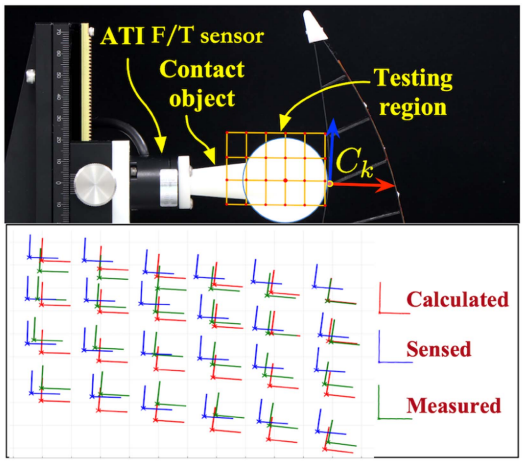

Fig. 11. Validation experiments for the sensing of contact locations.

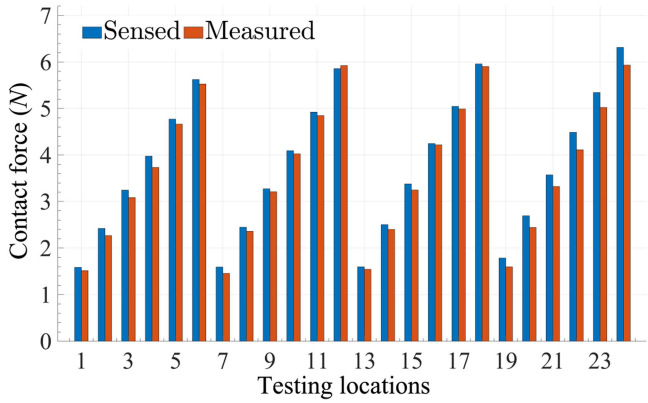

Fig. 12. Validation experiments for the sensing of contact forces.

In addition, the interaction force reacted between the object and the finger is predicted using the contact sensing method. Comparing with those measured by the force/torque sensor, the prediction errors of the sensed contact forces are provided in Fig. 12. From the results, it can be seen, using the proposed contact sensing method, the interaction force can be predicted effectively for the studied fin-ray finger composing of flexible components undergoing large deformations. As shown in the figure, the mean sensing error of contact forces at the tested locations is about 0.15 N (around 5% of the measured ones). This is comparatively high considering on the compactness of the sensors used for large-scale deformations.

To evaluate the sensing performance more comprehensively, the estimation accuracy for the contact condition is examined at different part of the developed adaptive gripper. As shown in Fig. 13, a variety of positions along the front side are selected and the manual stage is used to change the location of contact. For each height, several deformed configurations are tested to calculate the RMS error of the identified contact forces. The result of accuracy performance is given in Fig. 13. From the figure, it can be seen that the sensing accuracy at the finger's top and bottom part is much lower than that at the middle one. It is about $3 \sim 4$ times worse at the top/bottom part, which is

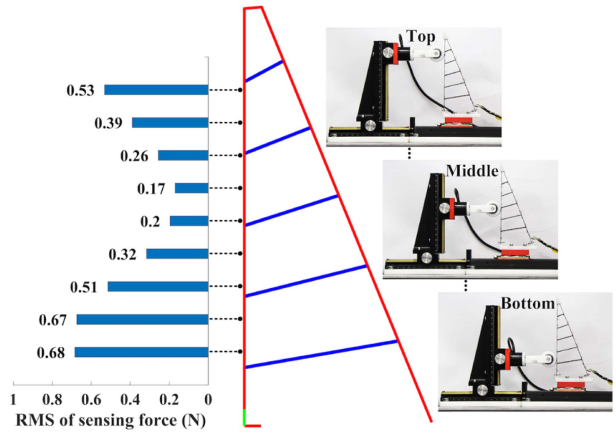

Fig. 13. Sensing accuracy of contact force at different part.

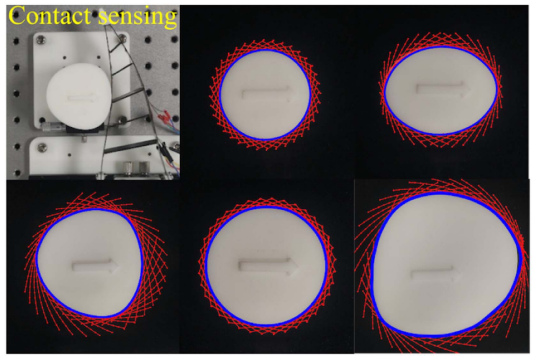

Fig. 14. Geometry reconstruction of objects with curved boundary.

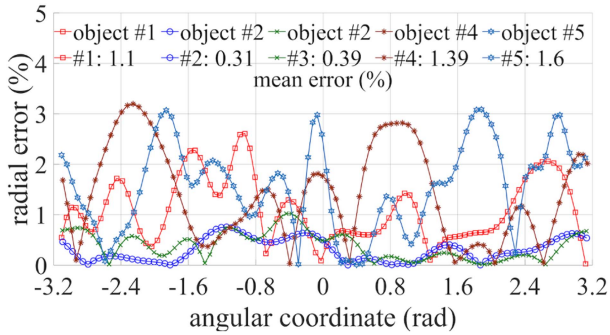

Fig. 15. Reconstruction accuracy of objects in curved boundary.

mainly caused by the difference of contact stiffness along the fin-ray structure. And it gives the users an intuitive view how to enhance the gripper's performance of contact sensing when performing interactive manipulation.

C. Validation of Object Geometry Reconstruction

In this section, validation experiments on shape construction of unknown objects are conducted on the developed adaptive fingers. As shown in Figs. 14 and 16, ten objects with different shapes are selected as candidates for geometry reconstruction.

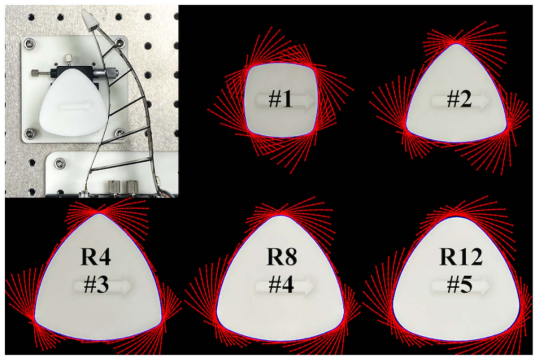

Fig. 16. Geometry reconstruction of objects with filleted corners.

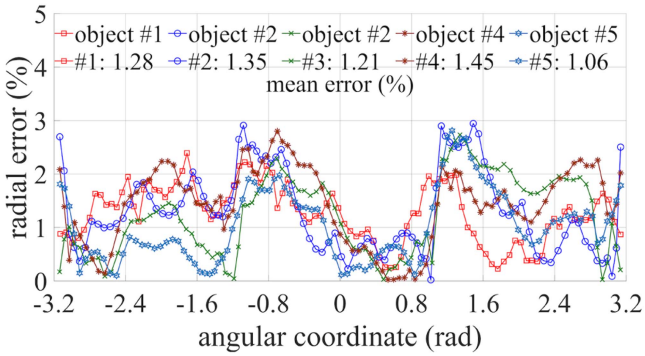

Fig. 17. Reconstruction accuracy of objects with fillet corners.

These testing objects could be divided into two categories with smoothly curved boundary and filleted corners, respectively.

For each object, 36 discrete orientations (with an increment of 10°) are evenly selected for the contact sensing, by manually rotating the object loading platform. Image processing technique is used to extract the contours of the testing objects from the gathered shape information about the local geometry. The results of geometry reconstruction are provided in Figs. 14 and 16, in an intuitive manner, with the direct comparison to the corresponding objects. From the results, it can be seen that, the reconstructed shapes of the tested objects fit the real ones pretty close. Even for those with filleted corners, the geometry around the local fillets can be reconstructed precisely using the proposed contact sensing method.

In addition, a quantitative assessment is provided to evaluate the accuracy performance of the proposed geometry reconstruction method. Polar coordinates are adopted to represent the boundary of the tested objects, and the prediction errors of their radial coordinate are provided in Figs. 15 and 17 for the two categories, respectively. The results indicate that the proposed contact sensing method is comparatively accurate for geometry reconstruction of unknown objects. The percentage errors of the identified radial coordinates are mostly less than 3% for all of the tested objects.

From the results, it is known that the estimation errors for the objects with filleted corners are slightly greater than those with smoothly curved boundaries. Moreover, the performance of reconstruction accuracy becomes even worse at the regions around the corners. This is mainly caused by the small radius of curvature at the filleted corners, which are relatively difficult to be identified, using the proposed single-point contact model. Overall, the developed adaptive fin-ray fingers with embedded compact deflection sensors perform pretty well in the geometry reconstruction of unstructured objects.

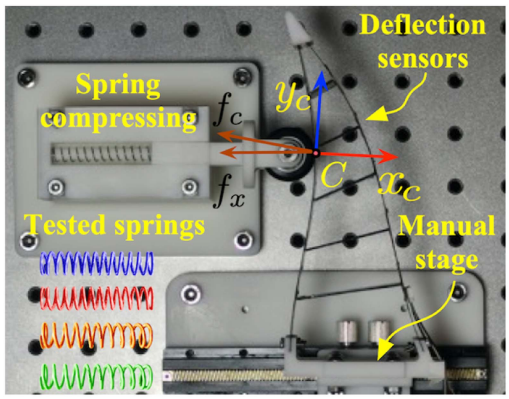

Fig. 18. Experimental setup of object compliance perception.

D. Validation of Object Compliance Perception

Based on the proposed sensing model, this section presents the validation experiments for the capability of perceiving structural compliance of unstructured objects. Following the idea presented in Section IV-C, a springy object-loading setup is particularly built up for this experiment. As shown in Fig. 18, five springs with different stiffness coefficients are tested on the developed adaptive gripper to validate the effectiveness of the proposed compliance perception method.

For each spring, five trials are held to identify the stiffness coefficient by means of pushing the finger towards the springy slider step by step. In each trial, 20 steps (1 mm for each) are taken to measure the corresponding compressing amount and contact force according to the proposed contact sensing model. The results are illustrated in Fig. 19, from which the stiffness coefficients of the tested springs can be specified in terms of the slope of the sensed force-compression lines. The identified stiffness coefficients are drawn in Fig. 19, in the form of a bar graph with error bars. Those measured by force sensor are provided in the figure as a reference of the springs' actual stiffness. From the results, it can be seen that, the developed fin-ray finger is capable of identifying the stiffness of the tested springs with an acceptable accuracy. The prediction errors of the stiffness coefficients are less than 15% with respect to the measured ones. Moreover, those with larger errors are of small stiffness, in which the friction of the loading slider and other unmodeled factors have comparatively large impact.

In addition, a demonstration for the capability of compliance perception of the developed adaptive gripper is performed on deformable objects. As shown in Fig. 20, six daily necessities, including a paper cup, a plastic water bottle, an aluminum soda can, a napkin package, and two silica-gel (one solid + another

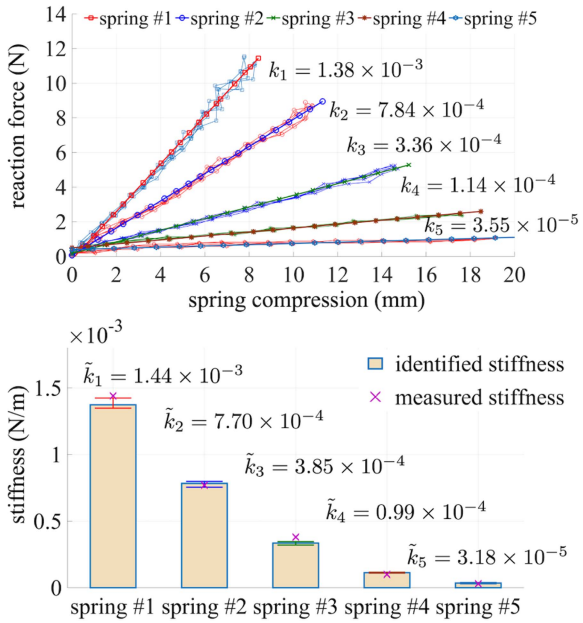

Fig. 19. Prediction accuracy of object compliance.

hollow) cylinders, are chosen for this intuitive demonstration. The developed two-finger gripper is used to manipulate these deformable objects actively, and meanwhile, the corresponding readings of the strain-gauge sensors that are integrated to the flexible beams are collected in real time.

Using the proposed contact sensing method, both the deformations of objects and the corresponding interactive forces can be identified and recorded during the whole grasping process. According to the force-deformation datum that gathered in the grasping trials, the compliance of the candidate objects can be evaluated and then, sorted. The result is illustrated in Fig. 20, in the sequence from the stiffest to the most compliant as: The solid silica-gel cylinder, the hollow one, the plastic bottle, the aluminum can, the napkin package, and the paper cup. For the sake of validation, compliance perception experiments on the same objects are also performed by some volunteers. The human-perceived results are as same as the one sorted via the proposed contact sensing method.

VI. Demonstration of Interactive Manipulation

Using the proposed sensing model, both the contact location and reaction force between the fin-ray finger and the object can be determined in real time. As a result, sensor-based feedback control can be implemented for the interactive manipulation of the developed adaptive gripper integrating compact deflection sensors. In this section, demonstrations on the control of contact force are provided to exhibit the capabilities of interactive grasping of the developed gripper.

To realize the sensor-based feedback control, a graphic user interface program is developed using the SoftBUS technique, as shown in Fig. 21, to integrate the deflection sensing, motor actuation, and kinetostatic calculation modules, as well as the commercial force sensor. As drawn in the figure, in the experimental setup, the fin-ray gripper is mounted on a linear stage actuated via a servo motor. Thus, the gripper's relative position to the object can be actively controlled (through the actuation module) to regulate the reaction force, which can be acquired according to the contact sensing model (through the calculation module) in light of the data sampled from the deflection sensors (via the sampling module). Meanwhile, the exact contact force is directly measured via the commercial force sensor (through the measuring module) to assess the accuracy of force control.

Based on the established setup, several scenarios of interactive manipulation are conducted to demonstrate the capability of contact force control of the fin-ray gripper developed in this work. In these experiments, the object is either mounted on a manual stage, or a motor-actuated linear stage to interact with the adaptive finger. First, validation experiments for real-time sensing of contact force are carried out. In this case, the finger is fixed on the linear stage, while the object is manually moved to interact with the finger in a dynamic way. The deformation of the fin-ray finger will change passively as the object moves. Then, the reaction force can be estimated using the proposed contact sensing model on the deformation datum collected by the deflection sensors. Owing to the integrated modules, this process can be implemented frequently. The sensing results of contact force are drawn in Fig. 22, in which those measured by the force sensor are also provided as a comparison.

From the results, it can be seen that the developed adaptive finger is able to predict the contact force in a continuous way. The sensing frequency of contact force can reach about 30 Hz using the developed experimental setup. In this experiment, the contact force reacted between the finger and the object changes from 0 to 8 N. And the root-mean-square (RMS) error of the estimated contact force is 0.18 N, with a maximum of 0.61 N. As exhibited in Fig. 22, four trials of "contacting-separating" cycles are carried out in an uninterrupted manner, and there is no evident differences in sensing performance between them. Actually, there is a small time interval between each two successive trials, when the finger is separated from the object. In this demonstration experiment, the time intervals between the trials are about 0.26, 0.77, and 0.14 s, respectively. As shown in Fig. 22, there is no evident difference in sensing performance between these trials. It implies that the adaptive grippers require very short time to recover from the deformed grasping configuration to the undeformed status. Thus, in the developed adaptive fin-ray gripper, the hysteresis of structural deformation is negligible for contact sensing.

On the basis of contact sensing capability, the contact force can be actively regulated on the developed experimental setup. In this case, the object on the manual stage is fixed, while the position of the adaptive soft finger is precisely controlled via the linear stage. In such a scenario, the contact force reacted between the object and the finger can be actively regulated by means of the sensor-based feedback control. Two prescribed trajectories, a harmonic and a step, are adopted to validate the proposed sensor-based feedback control for the contact force. Meanwhile, the exact contact force is also measured via the

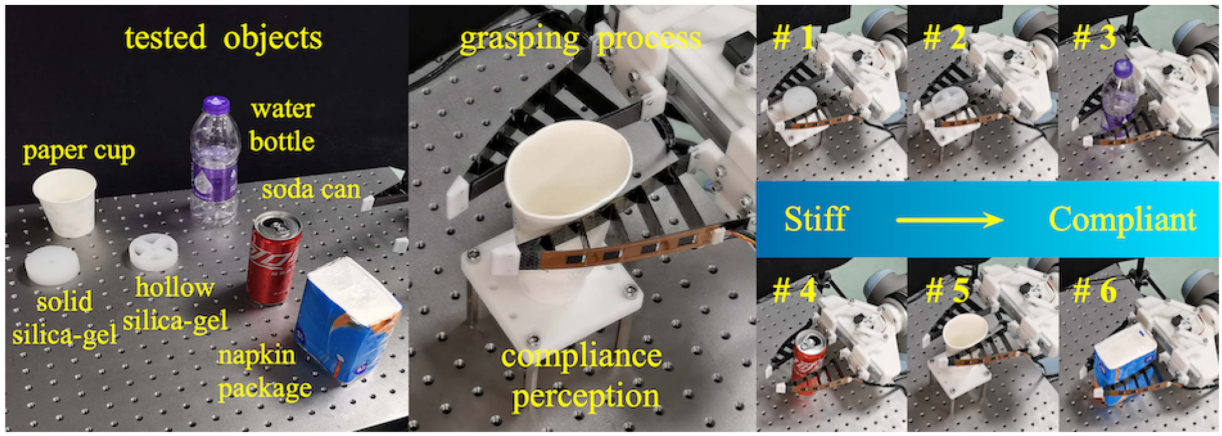

Fig. 20. Demonstration of the gripper's capability of object compliance for daily necessities.

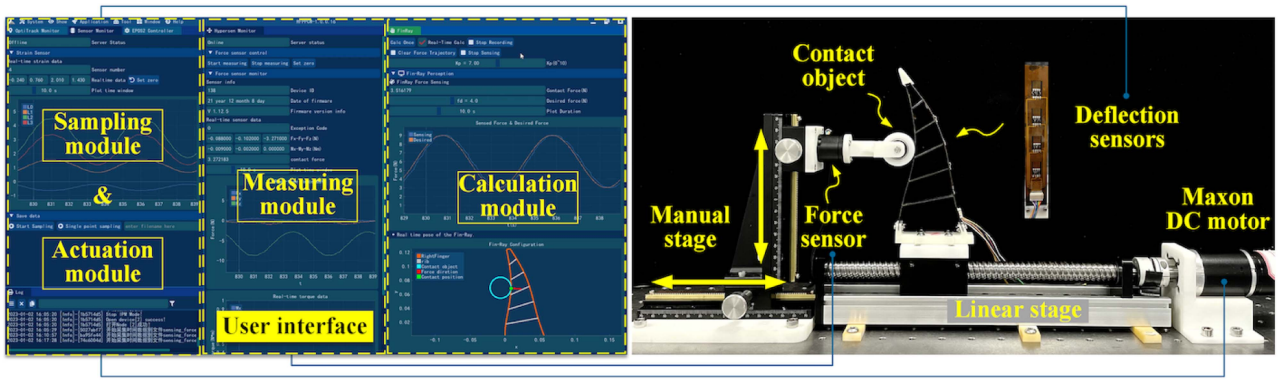

Fig. 21. Experimental setup of sensor-based feedback control for interactive manipulation.

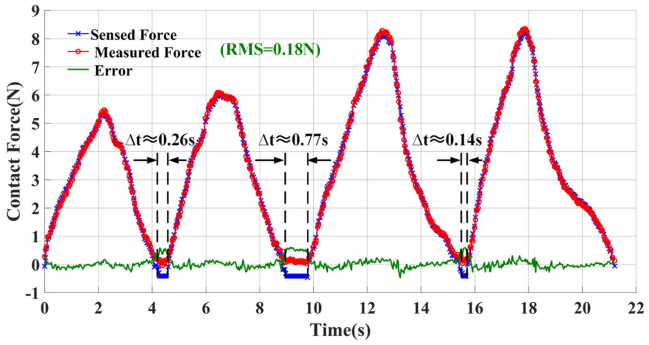

Fig. 22. Real-time sensing of contact force with a moving object.

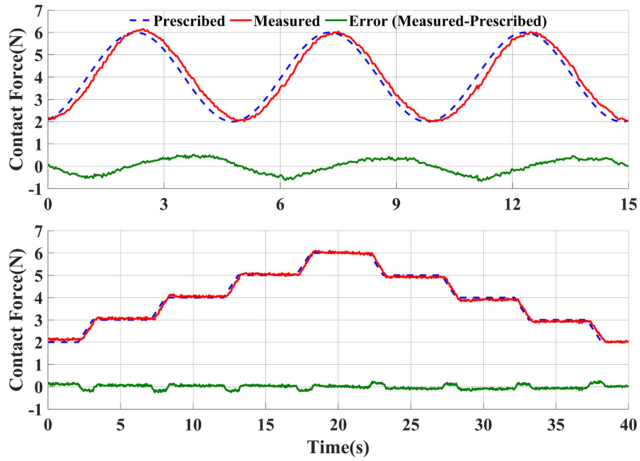

Fig. 23. Regulation of contact force along harmonic and step trajectories.

commercial force sensor to evaluate the performance of force control in contact with the static object.

The results are given in Fig. 23, in which the prescribed and measured trajectories of contact force are provided. As well, their differences are drawn in the figure, as the control errors of the contact force. From the results, it can be seen that the motor-actuated adaptive finger is able to realize active control of the contact force with the static object. The RMS errors of force control in the two prescribed trajectories are 0.32 N and 0.10 N, with the maximum of 0.65 N and 0.26 N, respectively. Moreover, there exists an obvious lag (about 130 ms) of the actual force with respect to the corresponding prescribed ones.

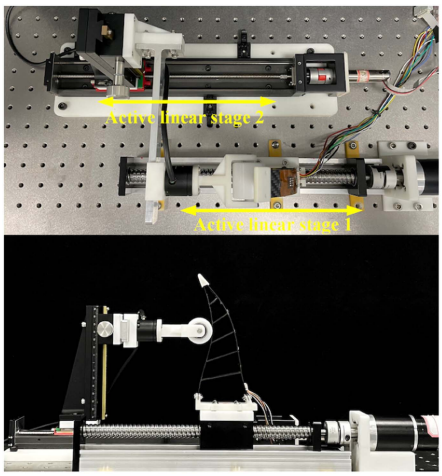

Fig. 24. Experimental setup for interactive force control with moving objects.

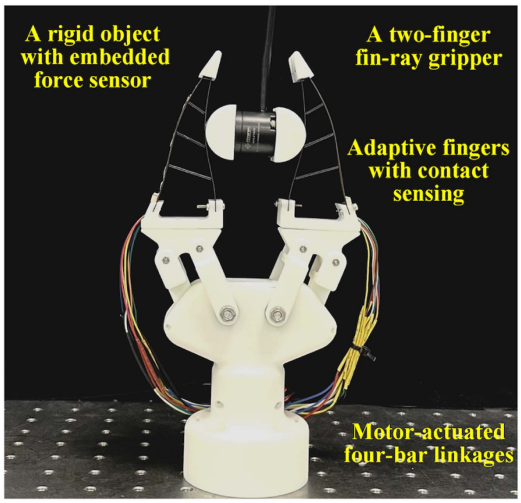

Fig. 26. Experimental setup of a two-finger gripper for interactive grasping.

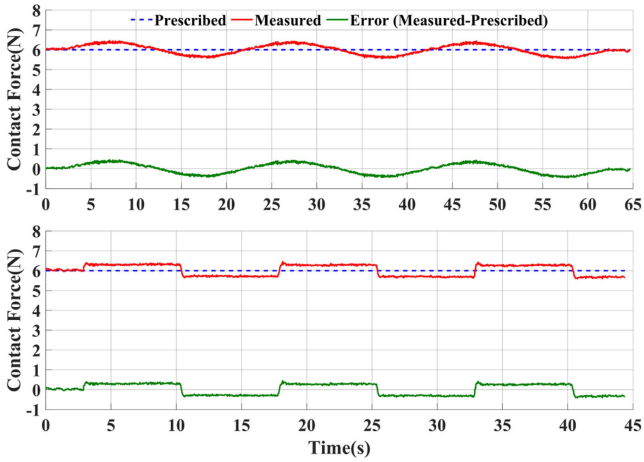

Fig. 25. Regulation of contact force with moving objects.

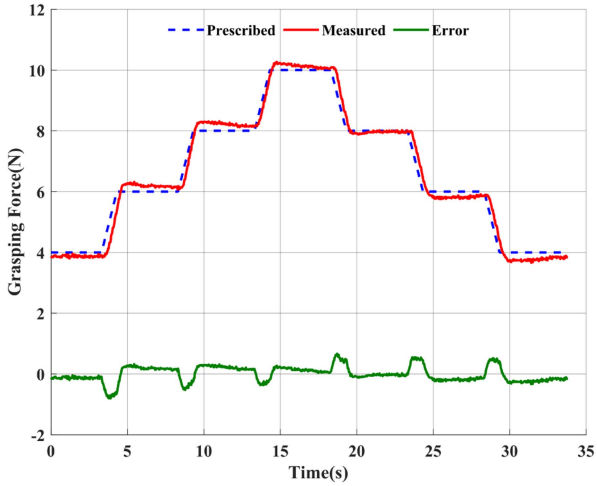

Fig. 27. Regulation of contact force in interactive grasping.

And this is mainly caused by the time delay between the actuation and calculation modules. Hence, the accuracy of force control of the developed adaptive fin-ray finger could be further improved by overcoming this issue, by means of using high-performance actuation strategy and hardware.

In addition to be in contact with a static object, interactive grasping with a moving object is conducted on the developed experimental setup. In this case, the object is also mounted on an active linear stage, which is individually actuated via a dc motor, as shown in Fig. 24. In this experiment, the position of the moving object is actively controlled in light of a prescribed trajectory, and the adaptive finger is actuated to be in contact with the object and stabilize the reaction force via the sensor-based feedback control. It should be noted that the prescribed motion of the object is unknown to the sensing and actuation system. In other words, the reaction force generated with the moving object is fully controlled according to the developed contact sensing method. Here, two trajectories, a harmonic and a triangular, are adopted to evaluate the capability of force control when following a moving object. The results are given in Fig. 25, from which it can be seen that the developed fin-ray gripper is able to regulate the contact force in a dynamic way. The RMS errors of force control are 0.25 N and 0.29 N (with the maximum 0.45 N and 0.46 N) for the harmonic and triangular motion, respectively. Comparing to the target force (6 N), the relative RMS error of the contact force is less than 5%, which is quite accurate for a soft gripper when performing an interactive manipulation with a moving object.

To demonstrate the capability of interactive grasping, a two-finger gripper is also developed, as shown in Fig. 26, which is actuated by one motor through two four-bar linkages. In this demonstration, a rigid object is grasped and manipulated by the gripper, which is capable of sensing the contact forces at both fingers. Thus, the grasping force can be actively adjusted by controlling the gripper's movement using the sensor-based feedback control scheme. In this experiment, a step trajectory, as drawn in Fig. 27, is prescribed for the gripper for interactive manipulation. And the grasping force is increased from 4 N to maximally 10 N (with a step of 2 N), and then decreased to

the initial state in an opposite way. In this case, the force sensor is internally embedded in the manipulated object, such that the actual grasping force can be measured directly as the reference. The results are provided in Fig. 27, from which it can be seen that, owing to the integration of deflection sensors, the developed fin-ray gripper is capable of sensing and controlling the grasping force that exerted on the manipulated object. The RMS error of the contact force is 0.25 N (with the maximum 0.80 N) when performing the interactive manipulation.

From the figure, it is obvious that the error of force control significantly increases when the gripper moves. This is because of the actuation delay generated in the control system and the physical mechanism. In those stable steps, th errors are only about half of the maximum, within 5% comparing to the corresponding prescribed ones. Therefore, the performance of force control during the interactive manipulation can be further improved by optimizing the strategies of feedback control and using the high-quality materials and fabrication techniques for prototyping. And this will be intensively studied in our future work to extend the developed capable-of-sensing adaptive gripper to interactive manipulation scenarios, such as force-guided assembling.

VII. Conclusion

In this article, a model-based intrinsic sensing method is proposed for the adaptive fin-ray gripper through the integration of compact deflection sensors. A discretization-based approach for the large deformation problems of flexible links is adopted to establish the kinetostatics model of the studied soft gripper consisting of coupled flexible and rigid components. Under the proposed modeling framework, a closed-form expression to the overall system Jacobian matrix of the kinetostatics model can be obtained in a straightforward way. Hence, the conventional Newton-Raphson method can be used to efficiently determine the large deformations of the soft fingers, and simultaneously, contact condition with the grasping objects. According to the deflection information gathered via the sensors, the developed fin-ray gripper is capable of sensing both the contact location and interaction force between the finger and the object.

Prototypes of the studied adaptive gripper are developed via easy-to-access materials and simple fabrication techniques. A variety of experiments are conducted to verify the feasibility and effectiveness of the proposed intrinsic sensing method for such fin-ray grippers. And the results show that the developed sensor-integrated adaptive gripper is able to predict the contact condition precisely. With this extra feature, the adaptive soft gripper can gather abundant information of the contact objects, for both geometry reconstruction and compliance perception, which has been validated through comprehensive experiments. An intuitive demonstration is also performed on the developed adaptive fin-ray gripper, in order to exhibit the capability of distinguishing deformable objects in light of their structural compliance. In addition, experiments of interactive manipulation are carried out to validate the capability of sensor-based feedback control of contact force. Using the proposed sensing model, the force reacted between the objects and the adaptive gripper can be actively regulated in contact with fixed, moving and grasping objects.

Appendix

A. System Jacobian Matrix of the Finger's Kinetostatics Model

The partial derivative item $\partial \boldsymbol{d}/\partial \boldsymbol{\theta}$ in (13) can be derived readily according to its definition as follows:

$$\frac{\partial \boldsymbol{d}}{\partial \boldsymbol{\theta}} = \begin{bmatrix} \boldsymbol{u}_1^T \frac{\partial}{\partial \boldsymbol{\theta}}(\boldsymbol{r}_{L_1} - \boldsymbol{r}_{R_1}) \\ \vdots \\ \boldsymbol{u}_n^T \frac{\partial}{\partial \boldsymbol{\theta}}(\boldsymbol{r}_{L_n} - \boldsymbol{r}_{R_n}) \end{bmatrix} = \begin{bmatrix} \boldsymbol{u}_1^T (\boldsymbol{\Gamma}_{L_1} \mathbf{J}_{L_1} - \boldsymbol{\Gamma}_{R_1} \mathbf{J}_{R_1}) \\ \vdots \\ \boldsymbol{u}_n^T (\boldsymbol{\Gamma}_{L_n} \mathbf{J}_{L_n} - \boldsymbol{\Gamma}_{R_n} \mathbf{J}_{L_n}) \end{bmatrix} \tag{21}$$

where $\boldsymbol{\Gamma}_{L_i} = [-\hat{\mathbf{r}}_{L_i}, \mathbf{I}_3] \in \mathbb{R}^{3\times 6}$ and $\boldsymbol{\Gamma}_{R_i} = [-\hat{\mathbf{r}}_{R_i}, \mathbf{I}_3] \in \mathbb{R}^{3\times 6}$. Here, $\hat{\mathbf{r}}_{L_i}$ and $\hat{\mathbf{r}}_{R_i}$ represent the 3×3 antisymmetric matrices of the vectors $\boldsymbol{r}_{R_i}$ and $\boldsymbol{r}_{L_i}$, respectively. $\mathbf{I}_3$ is the three-order identity matrix.

Similarly, the configuration-dependent item of the system's overall joint stiffness can be rewritten as follows:

$$\begin{aligned} \mathbf{K}_{\mathbf{J}} &= \frac{\partial}{\partial \boldsymbol{\theta}} \left(\mathbf{J}_t^T \boldsymbol{F}_t + \sum_{i=1}^{n} (\mathbf{J}_{L_i}^T - \mathbf{J}_{R_i}^T) \boldsymbol{F}_i \right) \\ &= \mathbf{K}_{\mathbf{J}_t} + \sum_{i=1}^{n} (\mathbf{K}_{\mathbf{J}_{L_i}} - \mathbf{K}_{\mathbf{J}_{R_i}}) + \sum_{i=1}^{n} f_i (\mathbf{J}_{L_i}^T - \mathbf{J}_{R_i}^T) \frac{\partial \boldsymbol{W}_i}{\partial \boldsymbol{\theta}} \end{aligned} \tag{22}$$

where the item $\mathbf{K}_{\mathbf{J}_{L_i}}$ and $\mathbf{K}_{\mathbf{J}_{R_i}}$ can be derived in the same way as the one of $\mathbf{K}_{\mathbf{J}_t}$.

The partial derivative of the unit wrench $\boldsymbol{W}_i$ with respect to $\boldsymbol{\theta}$ can be obtained as follows:

$$\frac{\partial \boldsymbol{W}_i}{\partial \boldsymbol{\theta}} = \begin{bmatrix} \hat{\mathbf{r}}_{L_i} \frac{\partial \boldsymbol{u}_i}{\partial \boldsymbol{\theta}} - \hat{\mathbf{u}}_i \frac{\partial \boldsymbol{r}_{L_i}}{\partial \boldsymbol{\theta}} \\ \frac{\partial \boldsymbol{u}_i}{\partial \boldsymbol{\theta}} \end{bmatrix}, \ i = 1, \ldots, n \tag{23}$$

where the item $\partial \boldsymbol{u}_i/\partial \boldsymbol{\theta}$ can be obtained in closed-form as $\partial \boldsymbol{u}_i/\partial \boldsymbol{\theta} = (\mathbf{I}_3 - \boldsymbol{u}_i \boldsymbol{u}_i^T)(\boldsymbol{\Gamma}_{L_i} \mathbf{J}_{L_i} - \boldsymbol{\Gamma}_{R_i} \mathbf{J}_{R_i})/d_i$. While $\partial \boldsymbol{r}_{L_i}/\partial \boldsymbol{\theta} = \boldsymbol{\Gamma}_{L_i} \mathbf{J}_{L_i}$ and $\partial \boldsymbol{r}_{R_i}/\partial \boldsymbol{\theta} = \boldsymbol{\Gamma}_{R_i} \mathbf{J}_{R_i}$ are as same as those in (21).

B. System Jacobian Matrix of the Contact Sensing Model

For the nonlinear algebraic equations of the contact sensing model (17), the system Jacobian matrix with respect to the unknown variables can be represented as follows:

$$\boldsymbol{\nabla}_{\boldsymbol{C}} = \begin{bmatrix} \mathbf{J}_t & \mathbf{0} & \mathbf{0} & \mathbf{0} & \mathbf{0} \\ \mathbf{K}_{\boldsymbol{\theta}} - \mathbf{K}_{\mathbf{J}} - \frac{\partial \mathbf{J}_c^T \boldsymbol{F}_c}{\partial \boldsymbol{\theta}} & -\mathbf{J}_t^T & \frac{\partial \boldsymbol{\tau}}{\partial \boldsymbol{f}} & \frac{\partial \boldsymbol{\tau}}{\partial l_c} & -\mathbf{J}_c^T \boldsymbol{W}_c \\ \frac{\partial \boldsymbol{d}}{\partial \boldsymbol{\theta}} & \mathbf{0} & \mathbf{0} & \mathbf{0} & \mathbf{0} \\ \mathbf{S}_e & \mathbf{0} & \mathbf{0} & \mathbf{0} & \mathbf{0} \end{bmatrix} \tag{24}$$

where only the two items $\partial(\mathbf{J}_c^T \boldsymbol{F}_c)/\partial \boldsymbol{\theta}$ and $\partial \boldsymbol{\tau}/\partial l_c$ require to be determined additionally.

In this case, the relative pose of the contact frame $\{\mathrm{C}\}$ can be represented as follows:

$$\mathbf{g}_{sc}(\boldsymbol{\theta}, l_c) = \exp(\hat{\boldsymbol{\zeta}}_1 \theta_1) \cdots \exp(\hat{\boldsymbol{\zeta}}_{n_c} \theta_{n_c}) \, \mathbf{g}_{c,0} \tag{25}$$

where $\mathbf{g}_{c,0}$ is the initial pose of $\{\mathrm{C}\}$ in the undeformed state, given by $\mathbf{g}_{c,0} = \{\mathbf{I}_3,\, l_c\, \boldsymbol{e}_2\}$, as shown in Fig. 7. $\boldsymbol{e}_2 = [0, 1, 0]^T$ is the unit vector associated with the $\boldsymbol{y}$-axis.

The additional item in the partial derivative $\frac{\partial \boldsymbol{\tau}}{\partial \boldsymbol{\theta}}$ that corresponds to the contact force can be derived as

$$\frac{\partial (\mathbf{J}_c^T \boldsymbol{F}_c)}{\partial \boldsymbol{\theta}} = \mathbf{K}_{\mathbf{J}_c} + f_c\, \mathbf{J}_c^T \frac{\partial \boldsymbol{W}_c}{\partial \boldsymbol{\theta}} \tag{26}$$

where $\mathbf{K}_{\mathbf{J}_c} \in \mathbb{R}^{N\times N}$ can be obtained in the same way as $\mathbf{K}_{\mathbf{J}_{L_k}}$. And the one of $\boldsymbol{W}_c$ with respect to $\boldsymbol{\theta}$ can be given by

$$\frac{\partial \boldsymbol{W}_c}{\partial \boldsymbol{\theta}} = \frac{\partial}{\partial \boldsymbol{\theta}} \left(\begin{bmatrix} \boldsymbol{r}_C \times \boldsymbol{x}_c \\ \boldsymbol{x}_c \end{bmatrix} \right) = \begin{bmatrix} \hat{\mathbf{r}}_C \boldsymbol{\Psi}_{\boldsymbol{x}_c} - \hat{\mathbf{x}}_c \boldsymbol{\Gamma}_{\boldsymbol{C}} \\ \boldsymbol{\Psi}_{\boldsymbol{x}_c} \end{bmatrix} \mathbf{J}_c \tag{27}$$

where $\boldsymbol{\Psi}_{\boldsymbol{x}_c} = [-\hat{\mathbf{x}}_c,\, \mathbf{0}_3] \in \mathbb{R}^{3\times 6}$ and $\boldsymbol{\Gamma}_{\boldsymbol{C}} = [-\hat{\mathbf{r}}_C,\, \mathbf{I}_3] \in \mathbb{R}^{3\times 6}$.

Similarly, the items $\partial \boldsymbol{\tau} / \partial l_c$ can be obtained directly as

$$\frac{\partial (\mathbf{J}_c^T \boldsymbol{F}_c)}{\partial l_c} = f_c\, \mathbf{J}_c^T \frac{\partial \boldsymbol{W}_c}{\partial l_c} = f_c\, \mathbf{J}_c^T \begin{bmatrix} \hat{\mathbf{r}}_C \boldsymbol{\Psi}_{\boldsymbol{x}_c} - \hat{\mathbf{x}}_c \boldsymbol{\Gamma}_{\boldsymbol{C}} \\ \boldsymbol{\Psi}_{\boldsymbol{x}_c} \end{bmatrix} \begin{bmatrix} \mathbf{0} \\ \boldsymbol{y}_c \end{bmatrix} \tag{28}$$

where $\boldsymbol{r}_C$ corresponds to the origin of $\{\mathrm{C}\}$. The unit vectors $\boldsymbol{x}_c$ and $\boldsymbol{y}_c$ relate to the directions of $\boldsymbol{x}$ and $\boldsymbol{y}$ axes of $\{\mathrm{C}\}$.

REFERENCES

[1] B. Siciliano and O. Khatib, *Springer Handbook of Robotics*. Berlin, Germany: Springer, 2008.

[2] J. Shintake, V. Cacucciolo, D. Floreano, and H. Shea, "Soft robotic grippers," *Adv. Mater.*, vol. 30, no. 29, 2018, Art. no. 1707035.

[3] F. Cini, V. Ortenzi, P. Corke, and M. Controzzi, "On the choice of grasp type and location when handing over an object," *Sci. Robot.*, vol. 4, no. 27, 2019, Art. no. eaau9757.

[4] J. Bohg, A. Morales, T. Asfour, and D. Kragic, "Data-driven grasp synthesis a survey," *IEEE Trans. Robot.*, vol. 30, no. 2, pp. 289–309, Apr. 2014.

[5] Z. Zhang, Y. Long, G. Chen, Q. Wu, H. Wang, and H. Jiang, "Soft and lightweight fabric enables powerful and high-range pneumatic actuation," *Sci. Adv.*, vol. 9, no. 15, 2023, Art. no. eadg1203.

[6] W. Crooks, G. Vukasin, M. O'Sullivan, W. Messner, and C. Rogers, "Fin ray® effect inspired soft robotic gripper: From the robosoft grand challenge toward optimization," *Front. Robot. AI*, vol. 3, p. 70, 2016.

[7] "Bionic tripod 3.0," 2011. [Online]. Available: https://www.festo.com/

[8] M. Wilson, "Festo drives automation forwards," *Assem. Automat.*, vol. 31, pp. 12–16, 2011.

[9] J. Hemming, C. Bac, B. Tuijl, R. Barth, J. Bontsema, and E. Pekkeriet, "A robot for harvesting sweet-pepper in greenhouses," in *Proc. Int. Conf. Argricalture Eng.*, Zurich, Switzerland, 2014.

[10] W. Crooks, "Soft robotic manipulators inspired by the fin ray effect," Ph.D. dissertation, Dept. Mech. Eng., Tufts Univ., Medford, MA, USA, 2017.

[11] R. Frisch-Fay, *Flexible Bars*. Washington, DC, USA: Butterworths, 1962.

[12] C. Kimball and L. Tsai, "Modeling of flexural beams subjected to arbitrary end loads," *J. Mech. Des.*, vol. 124, no. 2, pp. 223–235, 2002.

[13] A. Zhang and G. Chen, "A comprehensive elliptic integral solution to the large deflection problems of thin beams in compliant mechanisms," *J. Mechanisms Robot.*, vol. 5, no. 2, 2013, Art. no. 021006.

[14] L. Howell and A. Midha, "Parametric deflection approximations for end-loaded, large-deflection beams in compliant mechanisms," *ASME J. Mech. Des.*, vol. 117, no. 1, pp. 156–165, 1995.

[15] L. Howell, *Compliant Mechanisms*. New York, NY, USA: Wiley, 2001.

[16] H. Su, "A pseudo-rigid-body 3R model for determining large deflection of cantilever beams subject to tip loads," *J. Mechanisms Robot.*, vol. 1, no. 2, 2009, Art. no. 021008.

[17] L. Odhner and A. Dollar, "The smooth curvature model: An efficient representation of Euler-Bernoulli flexures as robot joints," *IEEE Trans. Robot.*, vol. 28, no. 4, pp. 761–772, Aug. 2012.

[18] F. Renda, F. Boyer, J. Dias, and L. Seneviratne, "Discrete Cosserat approach for multisection soft manipulator dynamics," *IEEE Trans. Robot.*, vol. 34, no. 6, pp. 1518–1533, Dec. 2018.

[19] C. Black, J. Till, and C. Rucker, "Parallel continuum robots: Modeling, analysis, and actuation-based force sensing," *IEEE Trans. Robot.*, vol. 34, no. 1, pp. 29–47, Feb. 2018.

[20] S. Briot and A. Goldsztejn, "Singularity conditions for continuum parallel robots," *IEEE Trans. Robot.*, vol. 38, no. 1, pp. 507–525, Feb. 2022.

[21] K. Elgeneidy, A. Fansa, I. Hussain, and K. Goher, "Structural optimization of adaptive soft fin ray fingers with variable stiffening capability," in *Proc. IEEE 3rd Int. Conf. Soft Robot.*, 2020, pp. 779–784.

[22] P. Manoonpong et al., "Fin Ray crossbeam angles for efficient foot design for energy-efficient robot locomotion," *Adv. Intell. Syst.*, vol. 4, no. 1, 2022, Art. no. 2100133.

[23] X. Shan and L. Birglen, "Modeling and analysis of soft robotic fingers using the Fin Ray effect," *Int. J. Robot. Res.*, vol. 39, no. 14, pp. 1686–1705, 2020.

[24] C. Armanini, I. Hussain, M. Iqbal, D. Gan, D. Prattichizzo, and F. Renda, "Discrete cosserat approach for closed-chain soft robots: Application to the Fin-Ray finger," *IEEE Trans. Robot.*, vol. 37, no. 6, pp. 2083–2098, Dec. 2021.

[25] R. Dahiya, G. Metta, M. Valle, and G. Sandini, "Tactile sensing - from humans to humanoids," *IEEE Trans. Robot.*, vol. 26, no. 1, pp. 1–20, Feb. 2010.

[26] M. Abdeetedal and M. Kermani, "Grasp and stress analysis of an underactuated finger for proprioceptive tactile sensing," *IEEE/ASME Trans. Mechatron.*, vol. 23, no. 4, pp. 1619–1629, Aug. 2018.

[27] C. Basson and G. Bright, "Geometric conformity study of a fin ray gripper utilizing active haptic control," in *Proc. IEEE 15th Int. Conf. Control Automat.*, 2019, pp. 713–718.

[28] J. Gandarias, J. Gomez-de Gabriel, and A. Garcia-Cerezo, "Enhancing perception with tactile object recognition in adaptive grippers for human–robot interaction," *Sensors*, vol. 18, no. 3, 2018, Art. no. 692.

[29] Y. Mahsereci, S. Saller, H. Richter, and J. Burghartz, "An ultra-thin flexible CMOS stress sensor demonstrated on an adaptive robotic gripper," *IEEE J. Solid-State Circuits*, vol. 51, no. 1, pp. 273–280, Jan. 2016.

[30] Y. She, S. Liu, P. Yu, and E. Adelson, "Exoskeleton-covered soft finger with vision-based proprioception and tactile sensing," in *Proc. IEEE Int. Conf. Robot. Automat.*, 2020, pp. 10075–10081.

[31] W. Xu, H. Zhang, H. Yuan, and B. Liang, "A compliant adaptive gripper and its intrinsic force sensing method," *IEEE Trans. Robot.*, vol. 37, no. 5, pp. 1584–1603, Oct. 2021.

[32] D. De Barrie, M. Pandya, H. Pandya, M. Hanheide, and K. Elgeneidy, "A deep learning method for vision based force prediction of a soft Fin Ray gripper using simulation data," *Front. Robot. AI*, vol. 8, 2021, Art. no. 631371.

[33] G. Chen, H. Wang, Z. Lin, and X. Lai, "The principal axes decomposition of spatial stiffness matrices," *IEEE Trans. Robot.*, vol. 31, no. 1, pp. 191–207, Feb. 2015.

[34] M. Hayley, T. Fatma, D. Neel, K. Je-sung, and W. Robert, "The millidelta: A high-bandwidth, high-precision, millimeter-scale delta robot," *Sci. Robot.*, vol. 3, no. 14, 2018, Art. no. eaar3018.

[35] J. Wang, G. Chen, and Z. Zhang, "Wireless multiplexing control based on magnetic coupling resonance and its applications in robot," *J. Mechanisms Robot.*, vol. 14, no. 1, 2022, Art. no. 011009.

[36] G. Chen, Z. Zhang, and H. Wang, "A general approach to the large deflection problems of spatial flexible rods using principal axes decomposition of compliance matrices," *J. Mechanisms Robot.*, vol. 10, no. 3, 2018, Art. no. 031012.

[37] G. Chen, H. Wang, and Z. Lin, "Determination of the identifiable parameters in robot calibration based on the POE formula," *IEEE Trans. Robot.*, vol. 30, no. 5, pp. 1066–1077, Oct. 2014.

[38] J. Selig, *Geometric Fundamentals of Robotics*. Berlin, Germany: Springer, 2005.

[39] G. Chen, Z. Zhang, L. Kong, and H. Wang, "Analysis and validation of a flexible planar two degrees-of-freedom parallel manipulator with structural passive sompliance," *J. Mechanisms Robot.*, vol. 12, no. 1, 2020, Art. no. 011011.

[40] G. Chen, Y. Kang, Z. Liang, Z. Zhang, and H. Wang, "Kinetostatics modeling and analysis of parallel continuum manipulators," *Mechanism Mach. Theory*, vol. 163, 2021, Art. no. 104380.

[41] J. Luo, Y. Xun, J. Yao, G. Chen, and H. Wang, "Sensor-based reconstruction of slender flexible beams undergoing large-scale deflection," in *Proc. IEEE/RSJ Int. Conf. Intell. Robots Syst.*, 2022, pp. 6936–6943.

[42] G. Chen, Y. Chai, S. Tang, Y. Chen, L. Kong, and H. Wang, "A study on the flexible bricard mechanisms with plane-symmetric structure," *Mechanism Mach. Theory*, vol. 188, 2023, Art. no. 105404.

[43] C. Zahn and R. Roskies, "Fourier descriptors for plane closed curves," *IEEE Trans. Comput.*, vol. 100, no. 3, pp. 269–281, Mar. 1972.

Genliang Chen (Member, IEEE) received the B.S. and Ph.D. degrees in mechanical engineering from Shanghai Jiao Tong University (SJTU), Shanghai, China, in 2006 and 2014, respectively.

From 2016 to 2017, he was a Visiting Scholar with the Biomimetic and Dexterous Manipulation Laboratory, Stanford University, Stanford, CA, USA. He is currently a Professor with the META Robotics Institute, and the State Key Laboratory of Mechanical System and Vibration, SJTU. His research interests include mechanism design, robot kinematics and dynamics.

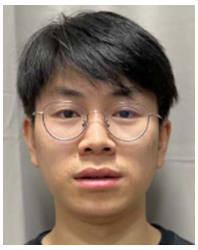

Shujie Tang received the B.S. degree in mechanical engineering from Chongqing University, Chongqing, China, in 2019. He is currently working toward the Ph.D. degree in mechanical engineering, with the META Robotics Institute, and the State Key Laboratory of Mechanical System and Vibration, Shanghai Jiao Tong University (SJTU), Shanghai, China.

His research interests include the elasto-dynamics modeling, analysis and control of continuum parallel robots.

Shaoqiu Xu received the B.S. degree in mechanical engineering from Tongji University, Shanghai, China, in 2019. He is currently working toward the master's degree in mechanical engineering, with the State Key Laboratory of Mechanical System and Vibration, and the Shanghai Key Laboratory of Digital Manufacture for Thin-walled Structures, Shanghai Jiao Tong University, Shanghai, China.

His research interests include the modeling, analysis, and synthesis of compliant grasping.

Tong Guan received the B.S. degree in mechanical engineering from Jilin University, Jilin, China, in 2020. He is currently working toward the master's degree in mechanical engineering, with the State Key Laboratory of Mechanical System and Vibration, and the Shanghai Key Laboratory of Digital Manufacture for Thin-walled Structures, Shanghai Jiao Tong University (SJTU), Shanghai, China.

His research interests include the dynamics modeling, analysis, and control of robotic systems.

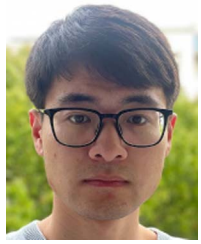

Yuanhao Xun received the B.S. degree in mechanical engineering from Central South University, Changsha, China, in 2019. He is currently working toward the master's degree in mechanical engineering, with the State Key Laboratory of Mechanical System and Vibration, and the Shanghai Key Laboratory of Digital Manufacture for Thin-walled Structures, Shanghai Jiao Tong University, Shanghai, China.

His research interests include the mechanism design, tactile sensing, and interactive control of flexible manipulators.

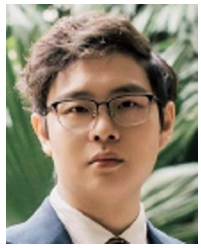

Zhuang Zhang (Member, IEEE) received the B.S. degree in mechanical engineering from Northeastern University, Shenyang, China, in 2015, and the Ph.D. degree in mechanical engineering from Shanghai Jiao Tong University, Shanghai, China, in 2021.

He is currently a Postdoctoral Research Fellow with the School of Engineering, Westlake University, Hangzhou, China. He has authored or coauthored more than 20 academic papers published in multidisciplinary/robotics journals and conferences, including *Nature Machine Intelligence, Nature Communications, Science Advances*, and ICRA. His research interests include origami robots and metamaterials, rigid-soft hybrid robots, mechanism design, and haptics.

Hao Wang received the B.S., M.S. and Ph.D. degrees from Tianjin University, Tianjing, China, in 1996, 1999 and 2002, respectively, all in mechanical engineering.

He is currently a Professor with the Shanghai Key Laboratory of Digital Manufacture for Thin-walled Structures, and the State Key Laboratory of Mechanical System and Vibration, Shanghai Jiao Tong University, Shanghai, China. His research interests include the mechanism design, multibody system dynamics, and smart manufacturing.

Zhongqin Lin received the M.S. and Ph.D. degrees in naval engineering and ship structural mechanics engineering from Shanghai Jiao Tong University, Shanghai, China, in 1986 and 1989, respectively.

He was elected as an Academician of the Chinese Academy of Engineering, Beijing, China, in 2011. He is currently the President of Shanghai Jiao Tong University. His research interests include quality control and process simulation technologies in auto-body manufacturing and their applications.